

Joint inversion of full-waveform GPR and ER data. Part 1

(October 31, 2019)

Running head: **Joint inversion of GPR and ER data. Part 1**

ABSTRACT

We develop an algorithm for joint inversion of full-waveform ground-penetrating radar (GPR) and electrical resistivity (ER) data. GPR is sensitive to electrical permittivity through reflectivity and velocity, and electrical conductivity through reflectivity and attenuation. ER is directly sensitive to electrical conductivity. The two types of data are inherently linked through Maxwell's equations and we jointly invert them. Results show that the two types of data work cooperatively to effectively regularize each other while honoring the physics of the geophysical methods. We first compute sensitivity updates separately for both the GPR and ER data using the adjoint method, and then we sum these updates to account for both types of sensitivities. The sensitivities are added with the paradigm of letting both data types always contribute to our inversion in proportion to how well their respective objective functions are being resolved in each iteration. Our algorithm makes no assumption of the subsurface geometry nor structural similarities between parameters with the caveat of needing a good initial model. We find that our joint inversion outperforms both GPR and ER separate inversions and determine that GPR effectively supports ER in regions of low conductivity while ER supports GPR in regions with strong attenuation.

INTRODUCTION

Imaging electrical properties (e.g. electrical permittivity ε and conductivity σ) is widely used for environmental and engineering applications. Contrasts in subsurface permittivity have been used to locate contaminant media (Bradford and Deeds, 2006; Babcock and Bradford, 2015), availability of water in the subsurface (Benedetto, 2010; Dogan et al., 2011; Parsekian et al., 2012), measure stratigraphy and volumetric water content in snow (Bradford et al., 2009; Sold et al., 2013; Schmid et al., 2014), find geologic structures (Kjær et al., 2018) and build hydrogeologic models for water-flow simulations (Knight, 2001). Subsurface conductivity has been used to quantify water content (Binley et al., 2002; Brunet et al., 2010; Beff et al., 2013), determine temperature distributions for geothermal exploration (Fikos et al., 2012; Hermans et al., 2012; Spichak and Zakharova, 2015), assess risk of landslides (Jomard et al., 2010; Perrone et al., 2014), monitor carbon-dioxide storage (Bergmann et al., 2012; Carrigan et al., 2013) and characterize mountain permafrost (Hauck et al., 2003; Scapozza et al., 2011; Rödder and Kneisel, 2012). Despite the broad range of applications for mapping electrical properties of the subsurface using GPR and ER methods, often a choice has to be made in using either method because of their contrasting sensitivities.

GPR is sensitive to electrical permittivity through reflectivity and velocity, and also sensitive to electrical conductivity through reflectivity and attenuation. However, if attenuation is strong in the media of interest the observed waveforms might not contain enough information to image either the permittivity or the conductivity. ER is directly (and only) sensitive to electrical conductivity, however if the media of interest has low conductivity, the measured data might not have enough information to give a meaningful image. Fortunately GPR and ER data have a complimentary relationship. GPR is sensitive to what ER is not

(permittivity) and ER is directly sensitive to what GPR is only sensitive by weak reflections and attenuation (conductivity). Moreover, GPR data gives a higher spatial resolution image of the media of interest in contrast with the lower spatial resolution obtained with the ER data.

Even though ray-theory methods for processing GPR data might resolve important features of the imaged media (Holliger et al., 2001; Bradford, 2006; Bradford et al., 2009), the caveat of only using the infinite frequency approximation of the data can lead to unsatisfactory results (Johnson et al., 2007; Linde and Vrugt, 2013). Introduced by Tarantola (1984) in the acoustic regime, full-waveform inversion of electromagnetic data has seen a steady interest for recovering electrical properties of the subsurface (see Ernst et al. (2007a) and Meles et al. (2010) for electromagnetic rather than acoustic full-waveform inversion). While many advances have been made for cross-hole data (Ernst et al., 2007a; Meles et al., 2010; Klotzsche et al., 2014; Gueting et al., 2017), using full waveform inversion for surface acquired GPR data in the presence of strong attenuative media remains an important challenge (Lavoué et al., 2014; Schmid et al., 2014).

In Lavoué et al. (2014) the authors perform full-waveform inversions of GPR on two synthetic examples, one with sources and receivers surrounding the target media and one with sources and receivers at the surface. When the target media is surrounded by sources and receivers they are able to recover accurate spatial resolution and values of the electrical parameters even when their starting models for both permittivity and conductivity are homogenous. However, when using surface acquired data the conductivity solution lacks accuracy and spatial resolution at shallow depths and is almost insensitive to sharp contrasts at depth. Moreover, in this case their starting models for both permittivity and conductivity are a smoothed version of the true parameters, which assumes a very accurate initial model

is available. The sharp difference in the resolution of the recovered parameters between these two synthetic experiments can be attributed to the sparse illumination due to having just surface acquired data, and shows how ill posed GPR full-waveform inversion can be when the conductivity is not known a priori.

ER inversion methods using the full response of the measured electric field range in how the data sensitivities are computed and in how the discretized physics are solved (Loke and Barker, 1996; Spitzer, 1998; Ha et al., 2006; Pidlisecky et al., 2007; Domenzain et al., 2017). Overall, the advances of the method have evolved in more accurate discretization schemes and computationally cheaper inversion routines. Because of the inherent low-spatial and shallow depth resolution of the ER data, sharp boundaries of the subsurface conductivity can be challenging to capture without external a priori knowledge of the subsurface or strong regularization (Hetrick and Mead, 2018).

In order to exploit the complimentary sensitivities of the GPR and ER experiments, we implement an inversion algorithm that recovers both permittivity and conductivity of the media of interest by joining the sensitivities of conductivity from both the GPR and ER data in each iteration of the inversion process. In what follows we make the physical assumptions of an isotropic linear media where Ohm’s law holds, with no lateral variation in the y -coordinate, a constant magnetic permeability of μ_o and frequency independent electrical parameters.

In recent work regarding GPR full-waveform inversion (Ernst et al., 2007a; Meles et al., 2010; Klotzsche et al., 2014; Lavoué et al., 2014; Gueting et al., 2017) it has been assumed that electrical conductivity is constant over a bandwidth of the radar signal and permittivity is frequency independent. Incorporating frequency dependent attenuation for

a full-waveform inversion approach can be done as in Xue et al. (2017), where the authors use a modified version of the wave equation (Zhu and Harris, 2014) and develop forward and adjoint operators that approximate the effects of frequency dependent attenuation. This enforces a higher computational cost compared to assuming frequency-constant attenuation. In Giannakis et al. (2015) the authors develop a 3d finite-difference time-domain forward model for electromagnetic wave propagation that incorporates frequency dependent parameters by convolving Debye relaxation mechanisms directly in the wave solver. Their forward model is capable of accurately predicting the behavior of electromagnetic fields with frequency dependent parameters but a full-waveform inversion algorithm that accounts for the convolution of relaxation mechanisms is still to be developed.

Recovering frequency dependent attenuation from surface acquired GPR data can be done as in Bradford (2007). The method links the attenuation coefficient to a dispersion relation that is measurable in the GPR data. It is noted that this method does not account for intrinsic vs scattering attenuation since it does not take into account the full kinematics of the electromagnetic wave. It is also recognized that because of the inability of GPR data to recognize reflections due to velocity from reflections due to conductive media, recovering the full attenuation response requires additional low frequency data. Using the full kinematic response of GPR on surface acquired data to recover attenuation is a very ill posed problem. As an example, see the results of Lavoué et al. (2014) on surface acquired data.

In Figure 1-**a**) and **b**) we present the real part of the frequency dependent effective conductivity as well as the DC conductivity. These values were computed using the Cole-Cole model with parameters given by Bradford (2007) (for sands and clay), Friel and Or (1999) (for silty loam) and Taherian et al. (1990) (for sandstone with brine). In general, the more conductive the material the larger the difference between DC and effective conductivity.

However, the larger the conductivity the less signal we have in the GPR data. Figure 1-d) shows that for high conductivity the skin factor drops below 1m as materials increase in conductivity. We note that for most earth materials, the DC and effective conductivity differs by a factor of less than an order of magnitude. In Table 1 we complete our list of materials with those in Loewer et al. (2017) (for humus, laterite and loess). We quantify how much this factor is at 250MHz and find that most earth materials differ by a factor of less than 5. Only dry sand (for this particular measured sample) exhibits a factor of 10, although the DC and effective conductivity are still low with 0.45 and 4.5 mS/m respectively.

We recognize that frequency independent electrical parameters are generally not true in nature. However, Figure 1 and Table 1 show that for a range of earth materials the frequency dependence varies by a small factor (less than 5 in most cases) and that in cases where the conductivity is large, the radar loses most of its signal due to attenuation. Assuming frequency dependent parameters forms a starting point for the evaluation of the algorithm and comprises a reasonable trade-off between computation cost, field applications, the full use of the GPR waveform, and a lack of enforced assumptions of subsurface geometry and petrophysical models.

Joining data from different types of geophysical imaging methods holds the promise of reducing the non-linearity of characterizing subsurface material properties (Ogunbo et al., 2018). Different approaches coupling the subsurface material properties as well as different algorithmic workflows have been developed in order to join different types of sensitivities (Moorkamp, 2017). Broadly, the material properties coupling can be done via geologic structure (where different material properties are assumed to share the same geometry (Haber and Oldenburg, 1997; Gallardo and Meju, 2003; Haber and Gazit, 2013)) or linked by petrophysical relationships (Ghose and Slob, 2006). More specifically, Linde et al. (2006)

use GPR and ER cross-hole data assuming structural similarities of electromagnetic properties and simplifying the physics of the GPR to only use travel times. Our approach for joint inversion does not assume structural similarities and does not need petrophysical relationships since the GPR and ER data are physically linked through conductivity with Maxwell's equations. We are able to increase the amplitude and spatial frequency resolution of the inverted electrical properties in a joint inversion compared with individual inversions of surface acquired data. In this way the GPR and ER optimization problems effectively regularize each other while honoring the physics.

The layout of the paper is as follows. In the subsections **GPR Inversion** and **ER Inversion** both the GPR and ER inversion schemes are developed separately and in Section **Joint Inversion** the method for joining the different sensitivities is described. In Section **Examples** we give results from our method with two different scenarios for underground exploration of surface acquisition: (1) low conductivity and (2) high conductivity, and present results with added noise in both the GPR and ER data.

INVERSION METHODS

GPR inversion

The physics of the GPR experiment are given by the time dependent Maxwell's equations,

$$\begin{pmatrix} \mu_o & 0 & 0 \\ 0 & \mu_o & 0 \\ 0 & 0 & \varepsilon \end{pmatrix} \begin{pmatrix} \dot{H}_z \\ -\dot{H}_x \\ \dot{E}_y \end{pmatrix} = \begin{pmatrix} 0 & 0 & \partial_x \\ 0 & 0 & \partial_z \\ \partial_x & \partial_z & 0 \end{pmatrix} \begin{pmatrix} H_z \\ -H_x \\ E_y \end{pmatrix} - \sigma \begin{pmatrix} 0 \\ 0 \\ E_y \end{pmatrix} + \begin{pmatrix} 0 \\ 0 \\ -J_y \end{pmatrix}, \quad (1)$$

where E_y is the electric field component in the y direction, (H_x, H_z) are the magnetic field components in the x and z direction, J_y is the source term, ε is the relative electrical permittivity (which we refer to only as permittivity), and σ is the electrical conductivity. Both ε and σ are assumed constant in time and frequency independent. In order to keep notation clean we will refer to operators and variables in capital and lower case letters respectively, and so refer to the wavefield E_y as u . Table 2 gives a comprehensive list of the notation symbols used in this paper. We use a finite-difference time-domain method on a Yee grid (Yee, 1966) with PML boundary conditions (Berenger, 1996) to solve the discretized time-domain (Domenzain et al., 2017) version of equation 1 which for reference we write as,

$$\begin{aligned} \mathbf{u} &= \mathbf{L}_w \mathbf{s}_w, \\ \mathbf{d}_w^s &= \mathbf{M}_w \mathbf{u} \end{aligned} \quad (2)$$

where \mathbf{L}_w is the discretized differential (time marching) operator of equation 1, \mathbf{u} is the electric field y component defined in space and time, \mathbf{s}_w is the source term, \mathbf{M}_w is the

measuring operator, and $\mathbf{d}_w^s = \mathbf{M}_w \mathbf{u}$ is the data of the experiment, i.e. a common-source gather. The operator \mathbf{M}_w formalizes the action of taking the data \mathbf{d}_w^s (a two-dimensional slice in time and receivers) from the three dimensional tensor \mathbf{u} with dimensions of time, length and depth. From now on ε and σ will denote the frequency independent electrical permittivity and conductivity distributions in the xz plane and discretized as matrices of size $n_z \times n_x$ where n_x and n_z denote the number of nodes in the xz -plane discretization.

We formulate our GPR inversion algorithm by finding parameters ε_* and σ_* that satisfy,

$$\{\varepsilon_*, \sigma_*\} = \arg \min \frac{1}{2} (\Theta_{w,\varepsilon}(\varepsilon; \mathbf{d}_w^o) + \Theta_{w,\sigma}(\sigma; \mathbf{d}_w^o)), \quad (3)$$

where the subscript $*$ denotes the imaged parameters and \mathbf{d}_w^o denotes all the observed GPR data. We have,

$$\Theta_{w,\varepsilon} = \frac{1}{n_s} \sum_s \Theta_{w,\varepsilon}^s, \quad (4)$$

where s indexes the sources, n_s denotes the total number of sources, and

$$\Theta_{w,\varepsilon}^s = \frac{\|\mathbf{e}_w\|_2^2}{\|\mathbf{d}_w^{o,s}\|_2^2}, \quad (5)$$

where $\mathbf{d}_w^{o,s}$ is the observed data for one source and $\mathbf{e}_w = \mathbf{d}_w^s - \mathbf{d}_w^{o,s}$ is the residual of the modeled and observed data. A similar expression for $\Theta_{w,\sigma}$ follows with the only difference between $\Theta_{w,\varepsilon}$ and $\Theta_{w,\sigma}$ being the order in the inversion scheme in which they are evaluated.

In order to find model updates $\Delta\sigma_w$ and $\Delta\varepsilon$ that minimize Θ_w we first obtain the gradients $\mathbf{g}_{w,\sigma}$ and \mathbf{g}_ε of $\Theta_{w,\varepsilon}^s$ and $\Theta_{w,\sigma}^s$ respectively following Meles et al. (2010) using a

full waveform inversion approach,

$$\mathbf{v}_w = \mathbf{L}_w \mathbf{e}_w(-t), \quad (6)$$

$$\mathbf{g}_{w,\sigma} = - \sum_t \mathbf{u}(-t) \odot \mathbf{v}_w(t) \cdot \Delta t, \quad (7)$$

$$\mathbf{g}_\varepsilon = - \sum_t \dot{\mathbf{u}}(-t) \odot \mathbf{v}_w(t) \cdot \Delta t, \quad (8)$$

where t denotes time, $(-t)$ denotes time reversed, \odot denotes element-wise multiplication, $\dot{\mathbf{u}}$ denotes the time derivative of \mathbf{u} (computed with in a finite-difference way), \mathbf{v}_w is the adjoint wavefield (the back-propagation of errors), and Δt denotes the discretized time interval. As noted by Kurzmann et al. (2013) using the adjoint method introduces high amplitude artifacts near the receivers that dominate the gradients. In order to remove these high amplitudes, we first multiply the gradients by a 2d gaussian surface in the xz -plane centered at the source location. The bandwidth of the 2d gaussian equals a wavelength where the wavelength is computed using the characteristic frequency of our survey and the velocity at the source location. We then apply a gaussian lowpass space-frequency filter following Taillandier et al. (2009) with the choice of bandwidth so as to only allow wavelengths larger than or equal to the characteristic wavelength of the model. The updates are,

$$\Delta \sigma_w = - \frac{1}{n_w} \sum_{s=1}^{n_w} \alpha_\sigma \mathbf{g}_{w,\sigma}, \quad (9)$$

$$\Delta \varepsilon = - \frac{1}{n_w} \sum_{s=1}^{n_w} \alpha_\varepsilon \mathbf{g}_\varepsilon, \quad (10)$$

where n_w is the number of GPR common-shot gathers and α_σ and α_ε are step-sizes for each gradient.

Even with a true descent direction $-\mathbf{g}_\varepsilon$, finding α_ε can be a very ill-posed inverse problem by itself leading to negative step-sizes, overshoot of the solution ε_* or a very slow

convergence. Overshooting the solution ε_* can lead to our current values of ε to fall outside the velocity interval determined by the stability conditions of our finite-difference wave solver both in time (Courant et al., 1967) and space (e.g. numerical dispersion).

For these reasons we choose to compute the step-size α_ε with a three-point parabola approximation of the objective function $\Theta_{w,\varepsilon}^s$ in the direction of its gradient (Wright and Nocedal, 1999). Each point used in the parabola approximation is the image of a perturbed permittivity $\hat{\varepsilon}_i$ under the objective function $\Theta_{w,\varepsilon}^s$,

$$\hat{\varepsilon}_i = \varepsilon \odot \exp(-\varepsilon \odot p_i \kappa_\varepsilon \cdot \mathbf{g}_\varepsilon), \quad i = 1, 2, 3, \quad (11)$$

where κ_ε is a positive real number and p_i is a fixed user defined percentage. At each iteration and for each source, κ_ε is chosen automatically in order to enforce the perturbed permittivity to lie within a certain range of possible values, i.e. within the stability velocity interval imposed by our wave solver (Courant et al., 1967) and we choose κ_ε to be as large as possible. We leave the details of finding κ_ε in **Appendix A**. Because at a given iteration we already have a value of $\Theta_{w,\varepsilon}^s$ for the current permittivity (i.e. with no perturbation), we choose p_i to be 0, 0.05 and 0.5. We proceed by computing $\Theta_{w,\varepsilon}^s(\hat{\varepsilon}_i; \mathbf{d}_w^{o,s})$ for $i = 1, 2, 3$ and then fitting a parabola through these points from which we analytically compute where the argument takes its minimum value: α_ε .

The computational cost of finding α_ε imposes one extra run of our forward model (equation 2) from what is done in Ernst et al. (2007b) and Meles et al. (2010), but proves to give more accurate values for the descent direction. We note that our search for κ_ε guarantees the permittivity values always lie within the stability conditions of our wave solver: both for the perturbations $\hat{\varepsilon}_i$ and the updated ε .

Because GPR is only sensitive to conductivity through attenuation and weak reflections,

in the case of strong attenuation the GPR data might not have enough information to constrain a parabolic shape on $\Theta_{w,\sigma}^s$ in the vicinity of the current parameters. We find the step-size α_σ by first finding the largest possible real number $\kappa_{w,\sigma}$ for which the perturbation in the direction of $-\kappa_{w,\sigma} \mathbf{g}_{w,\sigma}$ keeps the conductivity within a prescribed range of possible values. We then take a small percentage (in the order of 1%) of this value to be α_σ .

In late iterations we find that the updates in equation 9 can lead to an oscillatory exploration of the solution space. To mitigate this effect we impose a momentum m_ε (Rumelhart et al., 1986) to the descent direction $\Delta\varepsilon$,

$$\Delta\varepsilon \leftarrow \Delta\varepsilon + m_\varepsilon \Delta\varepsilon_\bullet, \quad (12)$$

where $\Delta\varepsilon_\bullet$ is the update of the previous iteration. The value of m_ε is kept constant throughout the inversion with a value of 25%.

At each iteration the updates are done in logarithmic scale in order to enforce the physical positivity constraint on both ε and σ ,

$$\varepsilon \leftarrow \varepsilon \odot \exp(\varepsilon \odot \Delta\varepsilon), \quad (13)$$

$$\sigma \leftarrow \sigma \odot \exp(\sigma \odot \Delta\sigma_w). \quad (14)$$

As noted by Meles et al. (2010), if the conductivity and permittivity reflections vary significantly it is not always convenient to compute the gradients and update under the same forward run. In lieu of this observation, in each iteration we first compute equation 2, we then compute $\Delta\varepsilon$ and update ε , we then compute our synthetic data (equation 2) again, compute $\Delta\sigma_w$ and update σ . In total, for each iteration for one source we compute equation 2 four times and equation 6 two times, which in total accounts for six forward models.

Assuming the source wavelet is known for all sources in our GPR experiment, we give

the algorithm for computing the updates $\Delta\epsilon$ and $\Delta\sigma_w$ in Figure 2. The full GPR inversion algorithm is given in Figure 4. The initialization of our algorithm consists in defining all constants used in our inversion and inputting a good initial guess for both permittivity and conductivity.

ER inversion

The physics of the ER experiment are given by the steady state Maxwell's equations where Ohm's law holds (Pidlisecky et al., 2007),

$$-\nabla \cdot \sigma \nabla \varphi = \mathbf{i}(\delta(x - s_+) - \delta(x - s_-)), \quad (15)$$

where φ is the electric potential, \mathbf{i} is the current intensity, s_{\pm} is the source-sink position, and σ is the electrical conductivity. Note that under our assumptions we are assuming that conductivity in equation 15 is the same as in equation 1. We write the discretized version of equation 15 as,

$$\begin{aligned} \mathbf{L}_{dc}\boldsymbol{\varphi} &= \mathbf{s}_{dc}, \\ \mathbf{d}_{dc}^s &= \mathbf{M}_{dc}\boldsymbol{\varphi}, \end{aligned} \quad (16)$$

where \mathbf{L}_{dc} is the discretized differential operator of equation 15, $\boldsymbol{\varphi}$ is the electric potential (a vector of size $n_x n_z \times 1$), \mathbf{s}_{dc} is the source term (a vector of size $n_x n_z \times 1$), \mathbf{M}_{dc} is the measuring operator that computes observed voltages (a matrix of size $n_{\mathbf{d}_{dc}^s} \times n_x n_z$ where $n_{\mathbf{d}_{dc}^s}$ denotes the number of measured voltages), and \mathbf{d}_{dc}^s is the data of the experiment for one source (a vector of size $n_{\mathbf{d}_{dc}^s} \times 1$).

We follow Dey and Morrison (1979) and use a finite volume method to build the discretized operator \mathbf{L}_{dc} , a sparse banded matrix of size $n_x n_z \times n_x n_z$ whose entries are a function of $\boldsymbol{\sigma}$ and the boundary conditions. Neumann boundary conditions are applied on

the air-ground interface, and Robin boundary conditions are applied in the subsurface (Dey and Morrison, 1979). By specifying Robin boundary conditions on the air-ground interface the matrix \mathbf{L}_{dc} is directly invertible. The source vector \mathbf{s}_{dc} is sparse having only ± 1 entries at the source and sink positions.

In order to directly compare the sensitivities of both experiments, we use the same discretized grid for both the GPR and the ER forward models. The spacings $\Delta x, \Delta z$ and Δt are determined by the Courant-Friedrichs-Lewy condition (Courant et al., 1967) with a user imposed interval of possible velocities in order for the GPR forward model to be numerically stable.

We formulate our ER inversion algorithm by finding $\boldsymbol{\sigma}_*$ that satisfies,

$$\boldsymbol{\sigma}_* = \arg \min \Theta_{dc}(\boldsymbol{\sigma}; \mathbf{d}_{dc}^o), \quad (17)$$

where \mathbf{d}_{dc}^o is all of the ER data. We have,

$$\Theta_{dc} = \frac{1}{n_s} \sum_s \Theta_{dc}^s, \quad (18)$$

where s indexes the source, n_s denotes the total number of sources, and

$$\Theta_{dc}^s = \frac{\|\mathbf{e}_{dc}\|_2^2}{\|\mathbf{d}_{dc}^{o,s}\|_2^2}. \quad (19)$$

We denote $\mathbf{d}_{dc}^{o,s}$ the observed data for one source and $\mathbf{e}_{dc} = \mathbf{d}_{dc}^s - \mathbf{d}_{dc}^{o,s}$ the residual of the modeled and observed data. In order to find the model update $\Delta \boldsymbol{\sigma}_{dc}$ that minimizes Θ_{dc}^s we first find the gradient of Θ_{dc}^s with respect to $\boldsymbol{\sigma}$. Let $\nabla_{\boldsymbol{\sigma}}$ be the vector of size $1 \times n_x n_z$ whose entries are the partial derivatives with respect to $\boldsymbol{\sigma}$. We compute \mathbf{g}_{dc} using the adjoint potential field \mathbf{v}_{dc} ,

$$\mathbf{L}_{dc}^\top \mathbf{v}_{dc} = \mathbf{M}_{dc}^\top \mathbf{e}_{dc}, \quad (20)$$

$$\mathbf{g}_{dc} = \mathbf{S}_{dc} \mathbf{v}_{dc},$$

where \mathbf{g}_{dc} and \mathbf{v}_{dc} are vectors of size $n_x n_z \times 1$ and $\mathbf{S}_{dc} = -((\nabla_{\sigma} \mathbf{L}_{dc}) \boldsymbol{\varphi})^{\top}$ is a matrix of size $n_x n_z \times n_x n_z$. We leave the details of this derivation for **Appendix B**.

Similarly to \mathbf{g}_{ε} and $\mathbf{g}_{w,\sigma}$, the gradient \mathbf{g}_{dc} exhibits strong amplitudes near the sources and receivers. We use the approach of Taillandier et al. (2009) to filter out these artifacts by applying a lowpass space-frequency domain gaussian filter with a choice of radius so as to only allow wavelengths larger or equal than the smallest source-receiver spacing.

Once the gradients for all sources have been computed the update is,

$$\Delta \boldsymbol{\sigma}_{dc} = -\frac{1}{n_{dc}} \sum_{s=1}^{n_{dc}} \alpha_{dc} \mathbf{g}_{dc}, \quad (21)$$

where n_{dc} is the number of ER experiments, and α_{dc} is a particular step size for each \mathbf{g}_{dc} . The step-size computations are done following Pica et al. (1990), where a perturbation $\hat{\boldsymbol{\sigma}}$ of $\boldsymbol{\sigma}$ in the direction of the gradient \mathbf{g}_{dc} is needed. We find the optimal perturbation parameter κ_{dc} such that,

$$\hat{\boldsymbol{\sigma}} = \boldsymbol{\sigma} \odot \exp(-\boldsymbol{\sigma} \odot \kappa_{dc} \mathbf{g}_{dc}), \quad (22)$$

using the same algorithm (but separately) as with the GPR inversion. Similarly to the GPR permittivity sensitivity, we add a percentage in the order of 10% of the previous iteration update to the current update $\Delta \boldsymbol{\sigma}_{dc}$ to avoid an oscillatory search of the solution space (Rumelhart et al., 1986),

$$\Delta \boldsymbol{\sigma}_{dc} \leftarrow \Delta \boldsymbol{\sigma}_{dc} + m_{dc} \Delta \boldsymbol{\sigma}_{dc \bullet}, \quad (23)$$

where $\Delta \boldsymbol{\sigma}_{dc \bullet}$ is the update from the previous iteration and m_{dc} is kept constant throughout the inversion. At each iteration the update is done in logarithmic scale in order to enforce the physical positivity constraint on $\boldsymbol{\sigma}$,

$$\boldsymbol{\sigma} \leftarrow \boldsymbol{\sigma} \odot \exp(\boldsymbol{\sigma} \odot \Delta \boldsymbol{\sigma}_{dc}). \quad (24)$$

We give the algorithm for computing the update $\Delta\sigma_{dc}$ in Figure 3. The full ER inversion algorithm is given in Figure 4. The initialization of our algorithm consists in defining all constants used in our inversion and inputting a good initial guess for conductivity.

JOINT INVERSION

We formulate our GPR and ER joint inversion algorithm by finding parameters $\boldsymbol{\varepsilon}_*$ and $\boldsymbol{\sigma}_*$ that satisfy,

$$\{\boldsymbol{\varepsilon}_*, \boldsymbol{\sigma}_*\} = \arg \min \frac{1}{2} (\Theta_{w,\varepsilon}(\boldsymbol{\varepsilon}; \mathbf{d}_w^o) + \Theta_{w,\sigma}(\boldsymbol{\sigma}; \mathbf{d}_w^o)) + \Theta_{dc}(\boldsymbol{\sigma}; \mathbf{d}_{dc}^o). \quad (25)$$

We optimize equation 25 by joining the updates $\Delta\sigma_w$ and $\Delta\sigma_{dc}$ obtained by equations 9 and 21 respectively. Since $\Delta\sigma_w$ and $\Delta\sigma_{dc}$ generally vary in magnitude, in order for the updates to share their different spatial sensitivities, we first normalize them by their largest amplitude and then add them together with scalar weights a_w and a_{dc} ,

$$\Delta\boldsymbol{\sigma} = a_w \Delta\boldsymbol{\sigma}_w + a_{dc} \Delta\boldsymbol{\sigma}_{dc}, \quad (26)$$

then normalize $\Delta\boldsymbol{\sigma}$ by its largest amplitude and finally write,

$$\Delta\boldsymbol{\sigma} \leftarrow c \Delta\boldsymbol{\sigma}, \quad (27)$$

where c is the geometric mean of the maximum amplitudes of $\Delta\boldsymbol{\sigma}_w$ and $\Delta\boldsymbol{\sigma}_{dc}$ prior to normalization. See Figure 5-a) for a summary of this procedure. The choices for weights a_w and a_{dc} are made with the paradigm of letting both updates $\Delta\boldsymbol{\sigma}_w$ and $\Delta\boldsymbol{\sigma}_{dc}$ always contribute to $\Delta\boldsymbol{\sigma}$ in proportion to their objective function value at a given iteration: if the objective function value of one is smaller than the other, then the one with the smaller

value should be more heavily weighted. The ad-hoc computation of a_w and a_{dc} is,

$$\begin{aligned}
 a_w &= \begin{cases} 1 & \text{if } h \Theta_{w,\sigma} \leq \Theta_{dc} \\ \frac{1}{\sqrt{|h \Theta_{w,\sigma} - (\Theta_{dc} - 1)|}} & \text{if } \Theta_{dc} < h \Theta_{w,\sigma}, \end{cases} \\
 a_{dc} &= \begin{cases} 1 & \text{if } \Theta_{dc} \leq h \Theta_{w,\sigma} \\ \frac{1}{\sqrt{|h \Theta_{w,\sigma} - (\Theta_{dc} + 1)|}} & \text{if } h \Theta_{w,\sigma} < \Theta_{dc}, \end{cases}
 \end{aligned} \tag{28}$$

where h is a positive number that further regulates the relative weight of GPR vs ER sensitivities. The value of h modulates how much we weigh each sensitivity: an increasing value of h decreases weighting of $\Delta\sigma_w$, while a decreasing value of h increases the weighting of $\Delta\sigma_w$.

Moreover, the choice of h over each iteration manages two aspects of the inversion: (a) at early iterations GPR data gives better sensitivity of sharp boundaries at shallow depths compared to the ER data so $\Delta\sigma_w$ should be weighed more, however at later iterations ER data gives better sensitivity overall so $\Delta\sigma_w$ should be weighed less. (b) We interpret an increase of Θ_{dc} (or $\Theta_{w,\sigma}$) with respect to the last iteration as a ‘‘cry for help’’ and so $\Delta\sigma_w$ should be weighed less (or more). Figure 6 shows the expected ‘‘bowtie’’ shape over iterations of a_w and a_{dc} that drives the physical sensitivities of our data in the parameter-space search-path.

Because the geometries of the hyper-surfaces defined by $\Theta_{w,\sigma}$ and Θ_{dc} as a function of σ are not known, we ensure the values of a_w and a_{dc} comply with the bowtie shape by enforcing emergent conditions (Cucker and Smale, 2007) that act individually on the magnitude of h , but when used together they interact into forming the bowtie shape. The conditions are (see Figure 5-b) for quick reference),

(0) We first choose a value of a_{dc} for the first iteration to be positive and smaller than 1 and force the first choice of h to comply with this initial value of a_{dc} .

(1) As the iterations proceed, if a_{dc} is decreasing we increase h by a fixed ratio \dot{a}_{dc} ,

$$h \leftarrow \dot{a}_{dc} h.$$

Note that a_{dc} can only decrease if a_w is 1.

(2) If a_w decreases we further force the descent of a_w increasing h by a fixed ratio \dot{a}_w ,

$$h \leftarrow \dot{a}_w h.$$

Note that the decrease of a_w begins when a_{dc} reaches 1.

In order to ensure the “cries for help” are listened at each iteration we enforce,

(3) If the value of Θ_{dc} increases with respect to the last iteration we increase h by a fixed ratio $\dot{\Theta}_{dc}$,

$$h \leftarrow \dot{\Theta}_{dc} h.$$

(4) If the value of $\Theta_{w,\sigma}$ increases with respect to the last iteration we decrease h by a fixed ratio $\dot{\Theta}_w$,

$$h \leftarrow \dot{\Theta}_w h.$$

In summary, the weight h regulates the current iteration’s choice of confidence over the sensitivities $\Delta\sigma_w$ and $\Delta\sigma_{dc}$, while the weights \dot{a}_{dc} , \dot{a}_w , $\dot{\Theta}_{dc}$ and $\dot{\Theta}_w$ regulate how h changes over each iteration. From conditions (1)-(4) we have,

$$\begin{aligned} \dot{a}_{dc} > 1 & \quad \dot{\Theta}_{dc} > 1 \\ \dot{a}_w > 1 & \quad \dot{\Theta}_w < 1. \end{aligned} \tag{29}$$

Because each condition **(1)**-**(4)** is tested at each iteration, more than one condition can be activated in the same iteration although not all combinations are possible, for example if **(1)** is activated then **(2)** is not since a_{dc} descending implies a_w is 1. Out of all the possible combinations of repeated conditions of **(1)**-**(4)**, only four are ambiguous in whether h increases or decreases, see equation 30. We solve the ambiguities involving GPR and ER terms by imposing an increase on h when they occur since this gives a higher weight on $\Delta\sigma_{dc}$ which is the update that is directly sensitive to the conductivity.

$$\begin{aligned}
\dot{a}_{dc} \dot{\Theta}_{dc} \dot{\Theta}_w &> 1 \\
\dot{a}_{dc} \dot{\Theta}_w &> 1 \\
\dot{a}_w \dot{\Theta}_{dc} \dot{\Theta}_w &> 1 \\
\dot{a}_w \dot{\Theta}_w &\geq 1
\end{aligned} \tag{30}$$

In practice we treat h as an invisible variable and only worry about finding values for $\dot{a}_{dc}, \dot{a}_w, \dot{\Theta}_{dc}$ and $\dot{\Theta}_w$ which remain constant throughout the inversion. These values are found empirically. Table 3 holds the designated roles of values $\dot{a}_{dc}, \dot{a}_w, \dot{\Theta}_{dc}$ and $\dot{\Theta}_w$. Table 4 holds the values used in our inversions for both low and high-conductivity scenarios.

The update for optimizing equation 25 is,

$$\sigma \leftarrow \sigma \odot \exp(\sigma \odot \Delta\sigma). \tag{31}$$

We summarize the procedure of computing the joint update $\Delta\sigma$ together with weight h in Figure 5.

EXAMPLES

Subsurface models

We illustrate our algorithm with two possible scenarios of the subsurface: one with low conductivity (σ between 1 and 4mS/m) and one with high conductivity (σ between 5 and 20mS/m) as shown in Figure 8. The permittivity is kept equal (but assumed unknown) in both scenarios. We place a box of size 1×1 m present in both permittivity and conductivity, and a reflector at depth with a 1m thickness present only in the permittivity. We invert for both permittivity and conductivity starting from homogeneous background models: $\sigma = 1$ mS/m and $\sigma = 4$ mS/m for the low and high conductivity scenarios respectively and $\varepsilon = 4$ for both scenarios.

The choice for the size of the box in our models is intended to stress our inversions as much as possible: large enough to have two wavelengths of the electromagnetic wave pass through, but small enough to be just within the minimum resolution of our ER acquisition sensitivity. We show the usefulness of the method on an exploration scenario relevant for field applications and simple enough for interpretation and assessment of our method.

Data acquisition

The GPR data are synthetically generated by applying 20 equally spaced sources (with a Ricker wavelet signature of 250MHz) on the air-ground interface with source-receiver spaced a wavelength away (≈ 0.5 m) and receiver-receiver distance a quarter of a wavelength away all along the air-ground interface. The ER data are also synthetically generated using 17 electrodes placed on the air-ground interface with one meter spacing between them and acquiring all possible dipole-dipole and Wenner array configurations.

Noise

We add white noise to our synthetic GPR common-source gathers with amplitude 10% of the standard deviation of each common-source gather (see Figure 9). We then lowpass the data up to 70% of our Nyquist frequency, which is where most of the noise spectra is shared with our noise-free data. Since the synthetic ER data do not follow a Gaussian distribution, we first cluster the data and then add white noise to each cluster with an amplitude of 10% of the standard deviation of each cluster (see Figure 10). We note that the noisy dipole-dipole array gathers exhibit a significant lower signal-to-noise ratio than the noisy Wenner array gathers, although we still use all of our noisy data for our inversions.

GPR inversions

In Figure 11-a) we see the recovered permittivity using just GPR data for the low conductivity scenario. We see the box correctly imaged and with values close to our true model while the bottom reflector is rightly imaged but the parameter value is not accurate because of amplitude loss in the data due to attenuation and two-way travel. We also observe low spatial frequency artifacts as a result of our surface source illumination with amplitudes dependent on the signal-to-noise ratio: with larger noise levels, the artifact amplitudes are recovered with a value closer to the permittivity of the box anomaly. For the high conductivity scenario (Figure 12-a)) the amplitude loss in the GPR data is even greater yielding speckle artifacts near the box of only 7.5% between the permittivity of the background and the box.

The lack of amplitude information due to attenuation of the GPR data is also appreciated in the recovered conductivities using only the GPR inversion as seen in Figure 13-a)

for the low conductivity and even more so in Figure 14-a) for the high conductivity. We note that because of the non-uniqueness between reflectivity caused by conductivity and that caused by permittivity, the GPR conductivity solution detects an artifact apparent boundary at the bottom of the model. High spatial frequency artifacts are also present in the recovered low conductivity.

ER inversions

The ER recovered conductivities shown in Figures 13-b) and 14-b) for the low and high-conductivity scenarios tell a different story from the GPR inversions: they have a more accurate amplitude detection, contain more low spatial frequencies (both in the detection of the box and the artifacts of the inversion), and because the ER data are directly and only sensitive to conductivity they do not contain the bottom reflector. We note however that because of our one-sided surface acquisition geometry and the inherent depth resolution of ER, the amplitude of the box decays in depth.

Joint inversions

The joint inversion recovered conductivities for the low and high scenarios are shown in Figures 13-c) and 14-c) respectively. We note improvements in the parameter accuracy and spatial resolution of the recovered conductivities compared to the GPR and ER inversions as well as a better depth resolution of the box. In Table 5 we quantify the improvement of our joint inversion by dividing the zero-lag crosscorrelation of the true and recovered conductivities with the zero-lag autocorrelation of the true conductivities. In both the low and high-conductivity scenarios we see an improvement over the separate GPR and ER

inversions. With respect to the GPR results, we improve by 3% and 5.4% in the low and high-conductivity scenarios respectively. With respect to the ER results, we improve by 0.11% in both the low and high-conductivity scenarios.

Because of the non-uniqueness of conductivity and permittivity reflections in the GPR data, our joint inversion has the caveat of detecting apparent boundaries in the conductivity solution. We also note artifacts in our joint inversion conductivities reminiscent of the artifacts in the GPR recovered permittivity around the box-anomaly (Figure 11-a)) although because of our weighting scheme that penalizes $\Delta\sigma_w$ in later iterations, these artifacts diminish amplitude as the number of iterations increase.

In the low conductivity scenario, Figure 15-a) shows that the GPR data dominates $\Delta\sigma$ for the first 4 iterations resolving sharp boundaries at shallow depths that $\Delta\sigma_{dc}$ is not yet sensitive to. However as iterations increase, $\Delta\sigma_w$ has contributed enough sensitivity for $\Delta\sigma_{dc}$ to resolve at depth and so the ER data dominates the inversion resolving the box and smoothing GPR high spatial frequency artifacts while still letting $\Delta\sigma_w$ contribute to the inversion. As shown in Figure 15-b) the first 20 iterations resolve the data at a faster pace than in later iterations.

Similar to the low-conductivity scenario, the ER data dominates most of the inversion as can be seen in Figure 16-a). Figure 16-b) shows a similar decrease of Θ_{dc} as in Figure 15-b) although Θ_w struggles to find a descent direction until the 40th iteration where both Θ_w and Θ_{dc} take a final descending stretch.

Because of the lack of information about the subsurface in the GPR data due to strong attenuation, the confidence of Θ_w in resolving the data is weak. The weak confidence of the GPR data is also seen in the small curvature of Θ_w : the changes in Θ_w are small compared

to the low conductivity scenario (Figure 15-b)), and the step sizes α_ε flip back and forth between positive and negative values throughout the inversion (not shown). The lack of curvature in Θ_w for the high conductivity scenario leads us to conclude that incorporating ER sensitivity to $\Delta\sigma_w$ is not enough to resolve permittivity.

In order to increase the resolution of permittivity values in the case of high conductivity, four possible solutions could be 1) using the low frequency information of the GPR in either a stepped frequency approach as in Meles et al. (2012); 2) changing the objective function in early iterations as in Bozdağ et al. (2011) or Ernst et al. (2007b) to allow for lower frequency content to be imprinted in both $\Delta\varepsilon$ and $\Delta\sigma_w$; 3) assuming the permittivity and conductivity geometric features are similar and using a cross-gradient approach as in Haber and Gazit (2013); Gallardo and Meju (2003) or 4) a joint update approach similar to equation 26 where instead of joining the GPR and ER conductivity sensitivities we join the permittivity ($\Delta\varepsilon$) and joint conductivity ($\Delta\sigma$) updates.

In Domenzain et al. (2019) we improve the resolution of our algorithm by incorporating the envelope of the GPR data and using the cross-gradients constraint in a single objective function.

CONCLUSIONS

We have developed a joint inversion algorithm for recovering subsurface frequency independent electrical permittivity and conductivity with surface acquisition and no assumed geometry or structure of the target media that enhances the sensitivity of the ground penetrating radar (GPR) and electrical resistivity (ER) data by introducing low and high spatial frequency information while honoring the physics of Maxwell equations. Our joint inversion

approach improves both the frequency independent permittivity and conductivity spatial and amplitude resolution of the target media compared with just GPR or ER inversions. Moreover, we find that GPR effectively supports ER in regions of low conductivity while ER supports GPR in regions with strong attenuation.

We perform an iterative non-linear inversion where the GPR and ER sensitivities are computed with the adjoint method and the conductivity GPR and ER sensitivities are joined with an ad-hoc method with the paradigm of letting both sensitivities always contribute to the inversion in proportion to how well their respective data are being resolved in each iteration. Our weighting method makes use of five fixed user defined values that further regulate the GPR and ER conductivity sensitivities automatically in each iteration, and that rely on the physical resolution of the GPR and ER experiments. Because our ad-hoc method to join the GPR and ER sensitivities is based on the value of the objective function values and the physical resolution of our geophysical methods, we suggest it can be used for joining other geophysical exploration methods where the physics involved play a similar role, e.g. active source seismic and gravity which are linked by density.

We assume the subsurface media is linear, isotropic, two dimensional and with frequency independent electrical parameters. In an effort to relax a-priori knowledge of the subsurface we do not use any petrophysical relationships throughout our work. These assumptions were chosen as a compromise between ease of computation cost and relevance with field data scenarios. Moreover, we note that for a variety of earth materials the DC and effective conductivity differ by a factor of less than an order of magnitude. Our assumptions enable us to directly couple the electrical conductivity sensitivities that the GPR and ER data are sensitive to. While frequency independent parameters are not true in general, it serves as a starting point for testing our algorithm and motivates the development of forward

models and inversion schemes that do take into account frequency dependency of electrical parameters.

In order to benchmark our algorithm we simulate GPR and ER data on two subsurface models, one with low (in the order of 10mS/m or less) and one with high (in the order of more than 10mS/m) conductivity. The low conductivity model was designed to test our algorithm in a case where the recovered permittivity is sufficiently resolved by the GPR data alone while the conductivity is only meaningfully recovered by the ER data. The high conductivity model was designed to test for a case where the GPR data alone cannot resolve a meaningful image of either permittivity or conductivity. Sources and receivers were placed on the air-ground interface simulating a real-data acquisition scenario for both GPR and ER experiments.

In both cases our joint inversion approach improves the resolution of spatial dimensions and amplitude of the target conductivity from just GPR and ER inversions. The spatial detection is measured as a ratio of zero-lag cross-correlations between true and recovered parameters. It is improved by 3% and 5.4% with respect to the GPR inversions in the low and high-conductivity scenarios respectively, and by 0.11% in both scenarios with respect to the ER inversions.

Because of the non-uniqueness between permittivity and conductivity reflections in the GPR data, our joint inversion scheme introduces apparent boundaries in the recovered conductivity that are not corrected with the ER data. High spatial frequency artifacts of the GPR sensitivity to the conductivity are mapped into our joint inversion solution, although these artifacts can be diminished in amplitude if the inversion is run for more iterations allowing for the low spatial frequency ER sensitivity to correct them. In both

low and high conductivity scenarios the recovered permittivity is not enhanced by using the ER sensitivity to conductivity, which can be of particular interest in the high conductivity case where permittivity is poorly solved by the GPR inversion.

Given the poor amplitude detection of the permittivity in the high conductivity scenario, approaches to increase the permittivity solution should likely 1) exploit low frequency content of the GPR data and 2) assume structural similarities of permittivity and conductivity. A possible path to enhance low frequency sensitivity of the GPR data could involve changing the objective function of the GPR inversion in early iterations or sequentially increase the frequency content of the GPR data during the inversion. If structural similarities between permittivity and conductivity are assumed, possible paths to accomplish 2) could be joining the conductivity sensitivities of the GPR and ER data in a cross-gradient scheme, or with a similar approach as presented in this paper for joining the GPR and ER conductivity sensitivities. In Part 2 we address 1) and 2) by enhancing our joint inversion with the envelope transform of the GPR data and cross-gradient constraints on both permittivity and conductivity.

Allowing for deeper spatial sensitivity for the ER experiment is equivalent to using long one-sided surface acquisition. In order to recover low frequencies and enough amplitude information from the GPR experiment, long one-sided surface acquisition of multi-offset data are needed. Given that our joint update for the conductivity assumes both updates are in the same spatial coordinates and with the same discretization, the cost for computing the GPR and ER forward models is increased from conventional GPR or ER experiments and inversion schemes. As a result, long offsets for both experiments are needed, yielding our approach best suited for shallow subsurface investigation.

Inverting for subsurface electrical properties using full-waveform of GPR data with data acquired on the surface is a new and emerging method. Choosing to carefully study synthetic examples where the solution is known enables us to assess the attributes and limitations of our method. This is an important step before using field data with our method because, in general, the solution of subsurface electrical parameters is unknown.

APPENDIX A

OPTIMALLY PERTURBING

Given a descent direction, finding the right step size is equivalent to traversing the objective function hyper-surface in the direction of the gradient ($-a \mathbf{g}_\varepsilon$) starting from our current value of ε and finding the value $a = \alpha_\varepsilon$ which minimizes the objective function (Wright and Nocedal, 1999). Traversing the objective function hyper-surface is done by perturbing the current value for ε with a collection of real numbers a_i . In equation 11 we used the notation $a_i = p_i \kappa_\varepsilon$ and gave empirical values for p_i . In this section we find κ_ε .

To speed-up convergence but maintain stability we perform a descending search for κ_ε . We start with a large value of κ_ε and compute the perturbation $\hat{\varepsilon}$,

$$\hat{\varepsilon} = \varepsilon \odot \exp(-\varepsilon \odot \kappa_\varepsilon \mathbf{g}_\varepsilon). \tag{A-1}$$

We then check if the minimum and maximum value of $\hat{\varepsilon}$ lie within our stability velocity region: if they do we have found κ_ε , if they do not we decrease κ_ε until they do. In practice once we have found a value of κ_ε that lies within our stability region, we repeat the search with finer ascending values of κ_ε to make sure $\hat{\varepsilon}$ is as snug as possible in our velocity interval.

APPENDIX B

ER GRADIENT

Taking the derivative with respect to $\boldsymbol{\sigma}$ and using the chain rule on the ER objective function for one source location,

$$\Theta_{dc}^s(\boldsymbol{\sigma}; \mathbf{s}_{dc}, \mathbf{d}_{dc}^{o,s}) = \frac{\|\mathbf{d}_{dc}^s - \mathbf{d}_{dc}^{o,s}\|_2^2}{\|\mathbf{d}_{dc}^{o,s}\|_2^2}, \quad (\text{B-1})$$

we have,

$$\nabla_{\boldsymbol{\sigma}} \Theta_{dc}^s = \nabla_{\mathbf{d}_{dc}^s} \Theta_{dc}^s \cdot \nabla_{\boldsymbol{\sigma}} \mathbf{d}_{dc}^s, \quad (\text{B-2})$$

where $\nabla_{\boldsymbol{\sigma}} \Theta_{dc}^s$ and $\nabla_{\mathbf{d}_{dc}^s} \Theta_{dc}^s$ are vectors of size $1 \times n_x n_z$ and $1 \times n_{\mathbf{d}_{dc}^s}$ respectively (where $n_{\mathbf{d}_{dc}^s}$ is the number of entries in the data) and $\nabla_{\boldsymbol{\sigma}} \mathbf{d}_{dc}^s$ is the Jacobian \mathbf{J}_{dc} of \mathbf{d}_{dc} , a matrix of size $n_{\mathbf{d}_{dc}^s} \times n_x n_z$. Because of our choice of Θ_{dc}^s to be the sum of square errors, $\nabla_{\mathbf{d}_{dc}^s} \Theta_{dc}^s$ is equal to \mathbf{e}_{dc}^\top . We make the convention of calling \mathbf{g}_{dc} the vertical vector whose entries are the partial derivatives of Θ_{dc}^s with respect to $\boldsymbol{\sigma}$, i.e. $\mathbf{g}_{dc} = (\nabla_{\boldsymbol{\sigma}} \Theta_{dc}^s)^\top$. We now take the transpose of equation B-2,

$$\mathbf{g}_{dc} = \mathbf{J}_{dc}^\top \mathbf{e}_{dc}. \quad (\text{B-3})$$

Our task will be to find a different expression for the right-hand side of equation B-3, (Domenzain et al., 2017; Pratt et al., 1998).

Using the product rule on equation 16, we have

$$\mathbf{L}_{dc} \nabla_{\boldsymbol{\sigma}} \boldsymbol{\varphi} + (\nabla_{\boldsymbol{\sigma}} \mathbf{L}_{dc}) \boldsymbol{\varphi} = 0. \quad (\text{B-4})$$

We now transpose equation B-4,

$$(\nabla_{\boldsymbol{\sigma}} \boldsymbol{\varphi})^\top \mathbf{L}_{dc}^\top = \mathbf{S}_{dc}, \quad (\text{B-5})$$

where $\mathbf{S}_{dc} = -((\nabla_{\sigma}\mathbf{L}_{dc})\boldsymbol{\varphi})^{\top}$ is a matrix of size $n_x n_z \times n_x n_z$ whose entries are explicitly calculated as a function of $\boldsymbol{\sigma}$, the spacial discretization and $\boldsymbol{\varphi}$. We define the adjoint field \mathbf{v}_{dc} to satisfy,

$$\mathbf{L}_{dc}^{\top} \mathbf{v}_{dc} = \mathbf{M}_{dc}^{\top} \mathbf{e}_{dc}, \quad (\text{B-6})$$

and multiply equation B-5 on the right side by \mathbf{v}_{dc} ,

$$\begin{aligned} (\nabla_{\sigma}\boldsymbol{\varphi})^{\top} \mathbf{L}_{dc}^{\top} \mathbf{v}_{dc} &= \mathbf{S}_{dc} \mathbf{v}_{dc}, \\ (\nabla_{\sigma}\boldsymbol{\varphi})^{\top} \mathbf{M}_{dc}^{\top} \mathbf{e}_{dc} &= \mathbf{S}_{dc} \mathbf{v}_{dc}, \\ (\nabla_{\sigma}\mathbf{d}_{dc}^s)^{\top} \mathbf{e}_{dc} &= \mathbf{S}_{dc} \mathbf{v}_{dc}, \\ \mathbf{J}_{dc}^{\top} \mathbf{e}_{dc} &= \mathbf{S}_{dc} \mathbf{v}_{dc}, \end{aligned} \quad (\text{B-7})$$

where in the second to last equality we have used $\nabla_{\sigma}\mathbf{d}_{dc}^s = \mathbf{M}_{dc} \nabla_{\sigma}\boldsymbol{\varphi}$. Finally we write,

$$\mathbf{g}_{dc} = \mathbf{S}_{dc} \mathbf{v}_{dc}. \quad (\text{B-8})$$

We note that this approach is similar to Pidlisecky et al. (2007), although we have explicitly written an expression for \mathbf{L}_{dc} and \mathbf{S}_{dc} entry by entry rather than as a multiplication of discretized differential operators, which yields full rank on \mathbf{L}_{dc} and \mathbf{S}_{dc} because of the used boundary conditions.

REFERENCES

- Babcock, E., and J. H. Bradford, 2015, Reflection waveform inversion of ground-penetrating radar data for characterizing thin and ultrathin layers of nonaqueous phase liquid contaminants in stratified media: *Geophysics*, **80**, H1–H11.
- Beff, L., T. Günther, B. Vandoorne, V. Couvreur, and M. Javaux, 2013, Three-dimensional monitoring of soil water content in a maize field using electrical resistivity tomography: *Hydrology and Earth System Sciences*, **17**, 595–609.
- Benedetto, A., 2010, Water content evaluation in unsaturated soil using gpr signal analysis in the frequency domain: *Journal of Applied Geophysics*, **71**, 26–35.
- Berenger, J.-P., 1996, Perfectly matched layer for the fdtd solution of wave-structure interaction problems: *IEEE Transactions on antennas and propagation*, **44**, 110–117.
- Bergmann, P., C. Schmidt-Hattenberger, D. Kiessling, C. Rücker, T. Labitzke, J. Henniges, G. Baumann, and H. Schütt, 2012, Surface-downhole electrical resistivity tomography applied to monitoring of co2 storage at ketzin, germany: *Geophysics*, **77**, B253–B267.
- Binley, A., G. Cassiani, R. Middleton, and P. Winship, 2002, Vadose zone flow model parameterisation using cross-borehole radar and resistivity imaging: *Journal of Hydrology*, **267**, 147–159.
- Bozdağ, E., J. Trampert, and J. Tromp, 2011, Misfit functions for full waveform inversion based on instantaneous phase and envelope measurements: *Geophysical Journal International*, **185**, 845–870.
- Bradford, J. H., 2006, Applying reflection tomography in the postmigration domain to multifold ground-penetrating radar data: *Geophysics*, **71**, K1–K8.
- , 2007, Frequency-dependent attenuation analysis of ground-penetrating radar data: *Geophysics*, **72**, J7–J16.

- Bradford, J. H., and J. C. Deeds, 2006, Ground-penetrating radar theory and application of thin-bed offset-dependent reflectivity: *Geophysics*, **71**, K47–K57.
- Bradford, J. H., J. T. Harper, and J. Brown, 2009, Complex dielectric permittivity measurements from ground-penetrating radar data to estimate snow liquid water content in the pendular regime: *Water resources research*, **45**.
- Brunet, P., R. Clément, and C. Bouvier, 2010, Monitoring soil water content and deficit using electrical resistivity tomography (ert)—a case study in the cevennes area, france: *Journal of Hydrology*, **380**, 146–153.
- Carrigan, C. R., X. Yang, D. J. LaBrecque, D. Larsen, D. Freeman, A. L. Ramirez, W. Daily, R. Aines, R. Newmark, J. Friedmann, et al., 2013, Electrical resistance tomographic monitoring of co2 movement in deep geologic reservoirs: *International Journal of Greenhouse Gas Control*, **18**, 401–408.
- Courant, R., K. Friedrichs, and H. Lewy, 1967, On the partial difference equations of mathematical physics: *IBM journal of Research and Development*, **11**, 215–234.
- Cucker, F., and S. Smale, 2007, Emergent behavior in flocks: *IEEE Transactions on automatic control*, **52**, 852–862.
- Dey, A., and H. Morrison, 1979, Resistivity modelling for arbitrarily shaped two-dimensional structures: *Geophysical Prospecting*, **27**, 106–136.
- Dogan, M., R. L. Van Dam, G. C. Bohling, J. J. Butler, and D. W. Hyndman, 2011, Hydrostratigraphic analysis of the made site with full-resolution gpr and direct-push hydraulic profiling: *Geophysical Research Letters*, **38**.
- Domenzain, D., J. Bradford, and J. Mead, 2017, Imaging by joint inversion of electromagnetic waves and DC currents: Presented at the SIAM Mathematical and Computational issues in the Geosciences.

- , 2019, Joint inversion of full-waveform gpr and er data. part 2: enhancing low frequencies with the envelope transform and cross-gradients: In review.
- Ernst, J. R., A. G. Green, H. Maurer, and K. Holliger, 2007a, Application of a new 2d time-domain full-waveform inversion scheme to crosshole radar data: *Geophysics*, **72**, J53–J64.
- Ernst, J. R., H. Maurer, A. G. Green, and K. Holliger, 2007b, Full-waveform inversion of crosshole radar data based on 2-d finite-difference time-domain solutions of maxwell’s equations: *IEEE transactions on geoscience and remote sensing*, **45**, 2807–2828.
- Fikos, I., G. Vargemezis, J. Zlotnicki, J. Puertollano, P. Alanis, R. Pigtain, E. Villacorte, G. Malipot, and Y. Sasai, 2012, Electrical resistivity tomography study of taal volcano hydrothermal system, philippines: *Bulletin of Volcanology*, **74**, 1821–1831.
- Friel, R., and D. Or, 1999, Frequency analysis of time-domain reflectometry (tdr) with application to dielectric spectroscopy of soil constituents: *Geophysics*, **64**, 707–718.
- Gallardo, L. A., and M. A. Meju, 2003, Characterization of heterogeneous near-surface materials by joint 2d inversion of dc resistivity and seismic data: *Geophysical Research Letters*, **30**.
- Ghose, R., and E. Slob, 2006, Quantitative integration of seismic and gpr reflections to derive unique estimates for water saturation and porosity in subsoil: *Geophysical Research Letters*, **33**.
- Giannakis, I., A. Giannopoulos, and C. Warren, 2015, A realistic fdtd numerical modeling framework of ground penetrating radar for landmine detection: *IEEE journal of selected topics in applied earth observations and remote sensing*, **9**, 37–51.
- Gueting, N., T. Vienken, A. Klotzsche, J. van der Kruk, J. Vanderborcht, J. Caers, H. Vereecken, and A. Englert, 2017, High resolution aquifer characterization using crosshole

- gpr full-waveform tomography: Comparison with direct-push and tracer test data: *Water Resources Research*, **53**, 49–72.
- Ha, T., S. Pyun, and C. Shin, 2006, Efficient electric resistivity inversion using adjoint state of mixed finite-element method for poisson’s equation: *Journal of Computational Physics*, **214**, 171–186.
- Haber, E., and M. H. Gazit, 2013, Model fusion and joint inversion: *Surveys in Geophysics*, **34**, 675–695.
- Haber, E., and D. Oldenburg, 1997, Joint inversion: a structural approach: *Inverse problems*, **13**, 63.
- Hauck, C., D. V. Mühll, and H. Maurer, 2003, Using dc resistivity tomography to detect and characterize mountain permafrost: *Geophysical prospecting*, **51**, 273–284.
- Hermans, T., A. Vandenbohede, L. Lebbe, and F. Nguyen, 2012, A shallow geothermal experiment in a sandy aquifer monitored using electric resistivity tomography: *Geophysics*, **77**, B11–B21.
- Hetrick, H., and J. Mead, 2018, Geophysical imaging of subsurface structures with least squares estimates: *Inverse Problems in Science and Engineering*, 1–20.
- Holliger, K., M. Musil, and H. Maurer, 2001, Ray-based amplitude tomography for crosshole georadar data: A numerical assessment: *Journal of Applied Geophysics*, **47**, 285–298.
- Johnson, T. C., P. S. Routh, W. Barrash, and M. D. Knoll, 2007, A field comparison of fresnel zone and ray-based gpr attenuation-difference tomography for time-lapse imaging of electrically anomalous tracer or contaminant plumes: *Geophysics*, **72**, G21–G29.
- Jomard, H., T. Lebourg, Y. Guglielmi, and E. Tric, 2010, Electrical imaging of sliding geometry and fluids associated with a deep seated landslide (la clapière, france): *Earth Surface Processes and Landforms: The Journal of the British Geomorphological Research*

- Group, **35**, 588–599.
- Kjær, K. H., N. K. Larsen, T. Binder, A. A. Bjørk, O. Eisen, M. A. Fahnestock, S. Funder, A. A. Garde, H. Haack, V. Helm, et al., 2018, A large impact crater beneath hiawatha glacier in northwest greenland: *Science advances*, **4**, eaar8173.
- Klotzsche, A., J. van der Kruk, J. Bradford, and H. Vereecken, 2014, Detection of spatially limited high-porosity layers using crosshole gpr signal analysis and full-waveform inversion: *Water Resources Research*, **50**, 6966–6985.
- Knight, R., 2001, Ground penetrating radar for environmental applications: *Annual Review of Earth and Planetary Sciences*, **29**, 229–255.
- Kurzmann, A., A. Przebindowska, D. Köhn, and T. Bohlen, 2013, Acoustic full waveform tomography in the presence of attenuation: a sensitivity analysis: *Geophysical Journal International*, **195**, 985–1000.
- Lavoué, F., R. Brossier, L. Métivier, S. Garambois, and J. Virieux, 2014, Two-dimensional permittivity and conductivity imaging by full waveform inversion of multioffset gpr data: A frequency-domain quasi-newton approach: *Geophysical Journal International*, **197**, 248–268.
- Linde, N., A. Binley, A. Tryggvason, L. B. Pedersen, and A. Revil, 2006, Improved hydrogeophysical characterization using joint inversion of cross-hole electrical resistance and ground-penetrating radar traveltimes data: *Water Resources Research*, **42**.
- Linde, N., and J. A. Vrugt, 2013, Distributed soil moisture from crosshole ground-penetrating radar travel times using stochastic inversion: *Vadose Zone Journal*, **12**.
- Loewer, M., T. Günther, J. Igel, S. Kruschwitz, T. Martin, and N. Wagner, 2017, Ultra-broad-band electrical spectroscopy of soils and sediments—a combined permittivity and conductivity model: *Geophysical Journal International*, **210**, 1360–1373.

- Loke, M. H., and R. Barker, 1996, Rapid least-squares inversion of apparent resistivity pseudosections by a quasi-newton method 1: Geophysical prospecting, **44**, 131–152.
- Meles, G., S. Greenhalgh, J. Van der Kruk, A. Green, and H. Maurer, 2012, Taming the non-linearity problem in gpr full-waveform inversion for high contrast media: Journal of Applied Geophysics, **78**, 31–43.
- Meles, G. A., J. Van der Kruk, S. A. Greenhalgh, J. R. Ernst, H. Maurer, and A. G. Green, 2010, A new vector waveform inversion algorithm for simultaneous updating of conductivity and permittivity parameters from combination crosshole/borehole-to-surface gpr data: IEEE Transactions on geoscience and remote sensing, **48**, 3391–3407.
- Moorkamp, M., 2017, Integrating electromagnetic data with other geophysical observations for enhanced imaging of the earth: a tutorial and review: Surveys in Geophysics, **38**, 935–962.
- Ogunbo, J. N., G. Marquis, J. Zhang, and W. Wang, 2018, Joint inversion of seismic travel-time and frequency-domain airborne electromagnetic data for hydrocarbon exploration: Geophysics, **83**, U9–U22.
- Parsekian, A. D., L. Slater, and D. Giménez, 2012, Application of ground-penetrating radar to measure near-saturation soil water content in peat soils: Water Resources Research, **48**.
- Perrone, A., V. Lapenna, and S. Piscitelli, 2014, Electrical resistivity tomography technique for landslide investigation: A review: Earth-Science Reviews, **135**, 65–82.
- Pica, A., J. Diet, and A. Tarantola, 1990, Nonlinear inversion of seismic reflection data in a laterally invariant medium: Geophysics, **55**, 284–292.
- Pidlisecky, A., E. Haber, and R. Knight, 2007, Resinvm3d: A 3d resistivity inversion package: Geophysics, **72**, H1–H10.

- Pratt, R. G., C. Shin, and G. Hick, 1998, Gauss–newton and full newton methods in frequency–space seismic waveform inversion: *Geophysical Journal International*, **133**, 341–362.
- Rödder, T., and C. Kneisel, 2012, Permafrost mapping using quasi-3d resistivity imaging, murtèl, swiss alps: *Near Surface Geophysics*, **10**, 117–127.
- Rumelhart, D. E., G. E. Hinton, and R. J. Williams, 1986, Learning representations by back-propagating errors: *nature*, **323**, 533.
- Scapozza, C., C. Lambiel, L. Baron, L. Marescot, and E. Reynard, 2011, Internal structure and permafrost distribution in two alpine periglacial talus slopes, valais, swiss alps: *Geomorphology*, **132**, 208–221.
- Schmid, L., A. Heilig, C. Mitterer, J. Schweizer, H. Maurer, R. Okorn, and O. Eisen, 2014, Continuous snowpack monitoring using upward-looking ground-penetrating radar technology: *Journal of Glaciology*, **60**, 509–525.
- Sold, L., M. Huss, M. Hoelzle, H. Anderegg, P. C. Joerg, and M. Zemp, 2013, Methodological approaches to infer end-of-winter snow distribution on alpine glaciers: *Journal of Glaciology*, **59**, 1047–1059.
- Spichak, V. V., and O. K. Zakharova, 2015, *Electromagnetic geothermometry*: Elsevier.
- Spitzer, K., 1998, The three-dimensional dc sensitivity for surface and subsurface sources: *Geophysical Journal International*, **134**, 736–746.
- Taherian, M., W. Kenyon, and K. Safinya, 1990, Measurement of dielectric response of water-saturated rocks: *Geophysics*, **55**, 1530–1541.
- Taillandier, C., M. Noble, H. Chauris, and H. Calandra, 2009, First-arrival travelttime tomography based on the adjoint-state method: *Geophysics*, **74**, WCB1–WCB10.
- Tarantola, A., 1984, Inversion of seismic reflection data in the acoustic approximation:

- Geophysics, **49**, 1259–1266.
- Wright, S., and J. Nocedal, 1999, Numerical optimization: Springer Science, **35**, 7.
- Xue, Z., J. Sun, S. Fomel, and T. Zhu, 2017, Accelerating full-waveform inversion with attenuation compensation: Geophysics, **83**, A13–A20.
- Yee, K., 1966, Numerical solution of initial boundary value problems involving maxwell's equations in isotropic media: IEEE Transactions on antennas and propagation, **14**, 302–307.
- Zhu, T., and J. M. Harris, 2014, Modeling acoustic wave propagation in heterogeneous attenuating media using decoupled fractional laplacians: Geophysics, **79**, T105–T116.

LIST OF TABLES

1 Frequency dependent and DC conductivities at 250MHz given by the Cole-Cole model. Most earth materials present an increase of at most 5 between DC and (real) effective conductivity.

2 Reference for the notation used in the discretized inverse problems. Symbols common in both GPR and ER experiments are stripped from their subscripts to avoid clutter.

3 Parameters for our joint inversions that were found empirically and remained fixed throughout the inversions. An increase in h favors $\Delta\sigma_{dc}$ more than $\Delta\sigma_w$. Conversely, a decrease in h favors $\Delta\sigma_w$ more than $\Delta\sigma_{dc}$.

4 Inversion parameters used for the low and high-conductivity scenario.

5 Ratio of maximum zero-lag cross-correlation between recovered and observed parameters for the low and high-conductivity scenarios. Closer to 1 is better. The joint inversion outperforms the GPR and ER recovered conductivities.

LIST OF FIGURES

1 Frequency dependent conductivity and attenuation coefficients of various earth materials. Solid and dashed lines represent (real) effective and DC conductivity respectively. In **a)** and **b)** are low conductivity materials where GPR data has a large signal-to-noise ratio. In **c)** and **d)** are high conductivity materials where GPR data has a low signal-to-noise ratio.

2 Algorithms for computing the updates $\Delta\epsilon$ and $\Delta\sigma_w$.

3 Algorithm for computing the update $\Delta\sigma_{dc}$.

4 Inversion algorithms for **a)** GPR and **b)** ER.

5 Algorithm for computing the update $\Delta\sigma$ as explained in Section **Joint Inversion**.

6 Diagram of weights a_w and a_{dc} as a function of iterations. An initial value for a_{dc} is chosen following condition **(0)**. If a_{dc} decreases over iterations, or Θ_{dc} increases, condition **(1)**, or **(3)**, are activated to increase a_{dc} . Once a_{dc} reaches the value 1, a_w is forced to steadily decrease with condition **(2)**. If $\Theta_{w,\sigma}$ increases over iterations, condition **(4)** is activated and a_w is increased but regulated by condition **(2)**.

7 Joint inversion algorithm as explained in Section **Joint Inversion**.

8 Subsurface models used for our inversions. The size of the box is 1×1 m. **a)** The permittivity background, bottom reflector and box have values of 4, 9 and 6 respectively. The conductivity background and box have values of 1 and 4 mS/m for the low conductivity **b)** and 4 and 20 mS/m for the high conductivity **c)** respectively. An example of GPR receivers and source are depicted in green and red in **b)** and ER electrodes are depicted in green in **c)**.

9 GPR data for one source noise free and with added noise.

10 **a)** All ER data noise free and the clusters used for adding noise depicted with

symbols $+$, \bullet , and \times . **b)** Pseudo-section of a dipole-dipole survey noise free and **c)** with added noise.

11 Recovered permittivity for the low-conductivity scenario with just GPR data **a)** and with GPR and ER data **b)**.

12 Recovered permittivity for the high-conductivity scenario with just GPR data **a)** and with GPR and ER data **b)**.

13 Recovered low conductivity using **a)** just GPR data, **b)** just ER data, and **c)** both GPR and ER data. Each inversion was run for 50 iterations.

14 Recovered high conductivity using **a)** just GPR data, **b)** just ER data, and **c)** both GPR and ER data. Each inversion was run for 50 iterations.

15 Update weights history over iterations for the low-conductivity scenarios **a)** and normalized objective functions history over iterations **d)**.

16 Update weights history over iterations for the high-conductivity scenarios **a)** and normalized objective functions history over iterations **d)**.

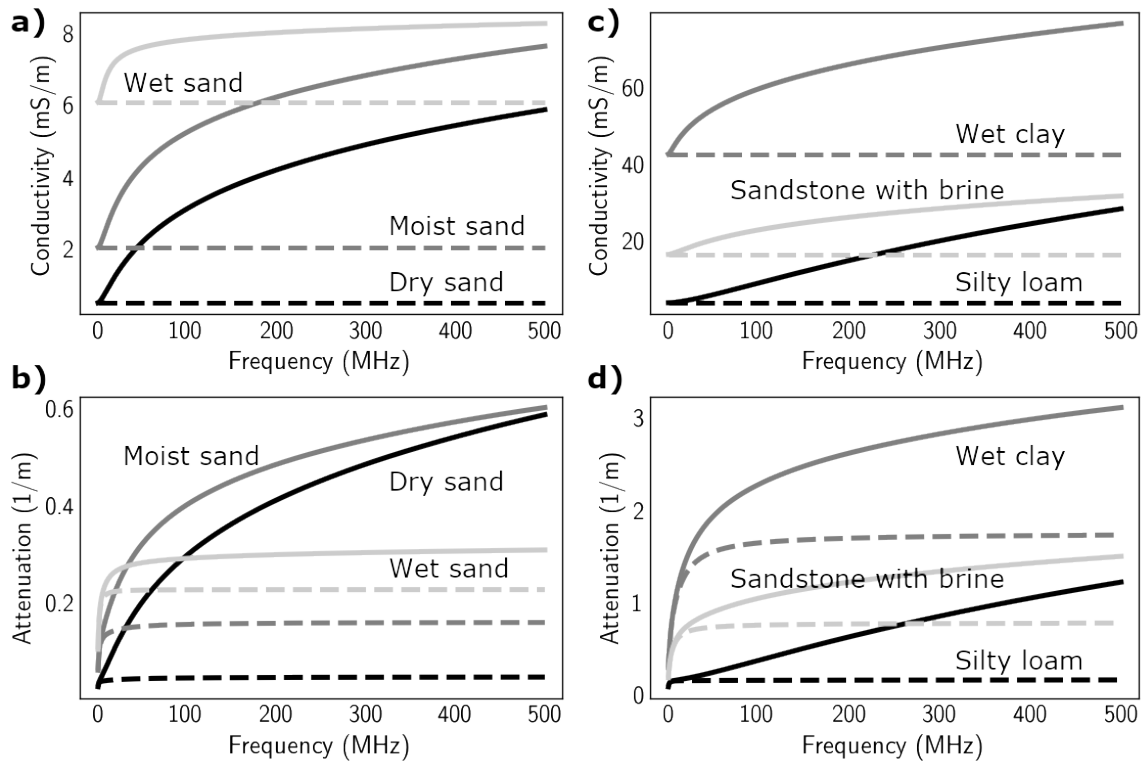


Figure 1: Frequency dependent conductivity and attenuation coefficients of various earth materials. Solid and dashed lines represent (real) effective and DC conductivity respectively. In **a)** and **b)** are low conductivity materials where GPR data has a large signal-to-noise ratio. In **c)** and **d)** are high conductivity materials where GPR data has a low signal-to-noise ratio.

	Effective (mS/m)	DC (mS/m)	Effective/DC
Dry sand	4.54	0.45	10.1
Moist sand	6.53	2	3.26
Wet sand	8.06	6.06	1.33
Silty loam	17.3	3.5	4.93
Sandstone with brine	27.2	16.2	1.68
Humus	43.1	19.5	2.21
Laterite	45	9	5
Wet clay	68.4	42.5	1.61
Loess	185	72.3	2.55

Table 1: Frequency dependent and DC conductivities at 250MHz given by the Cole-Cole model. Most earth materials present an increase of at most 5 between DC and (real) effective conductivity.

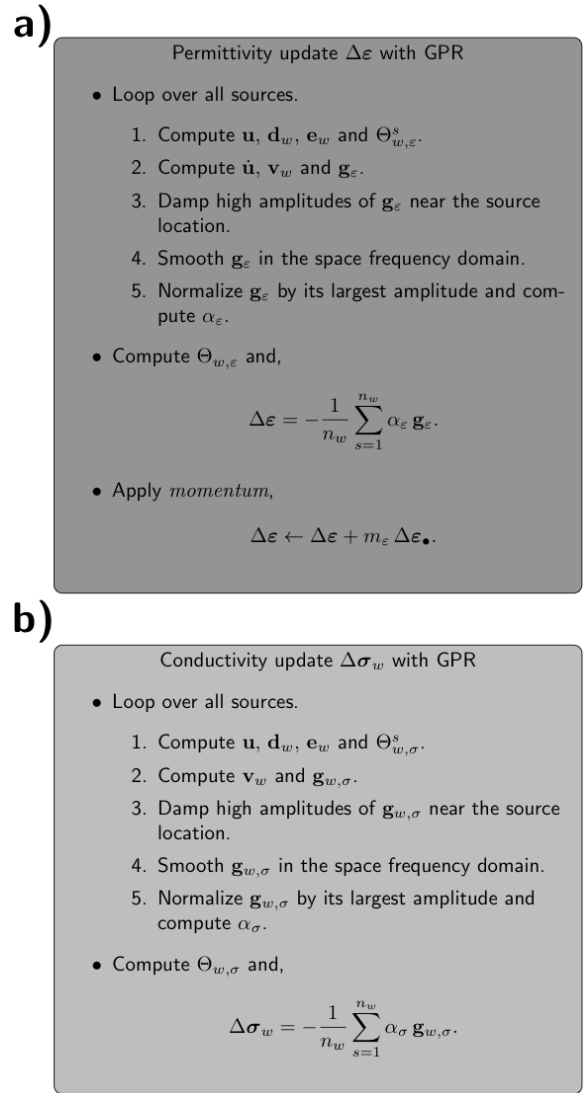


Figure 2: Algorithms for computing the updates $\Delta\epsilon$ and $\Delta\sigma_w$.

Conductivity update $\Delta\sigma_{dc}$ with ER

- Loop over all sources.
 1. Compute φ , \mathbf{d}_{dc} , \mathbf{e}_{dc} and Θ_{dc}^s .
 2. Compute \mathbf{v}_{dc} and \mathbf{g}_{dc} .
 3. Smooth \mathbf{g}_{dc} in the space frequency domain.
 4. Normalize \mathbf{g}_{dc} by its largest amplitude and compute α_{dc} .
- Compute Θ_{dc} and,

$$\Delta\sigma_{dc} = -\frac{1}{n_{dc}} \sum_{s=1}^{n_{dc}} \alpha_{dc} \mathbf{g}_{dc}.$$
- Apply *momentum*,

$$\Delta\sigma_{dc} \leftarrow \Delta\sigma_{dc} + m_{dc} \Delta\sigma_{dc}.$$

Figure 3: Algorithm for computing the update $\Delta\sigma_{dc}$.

-

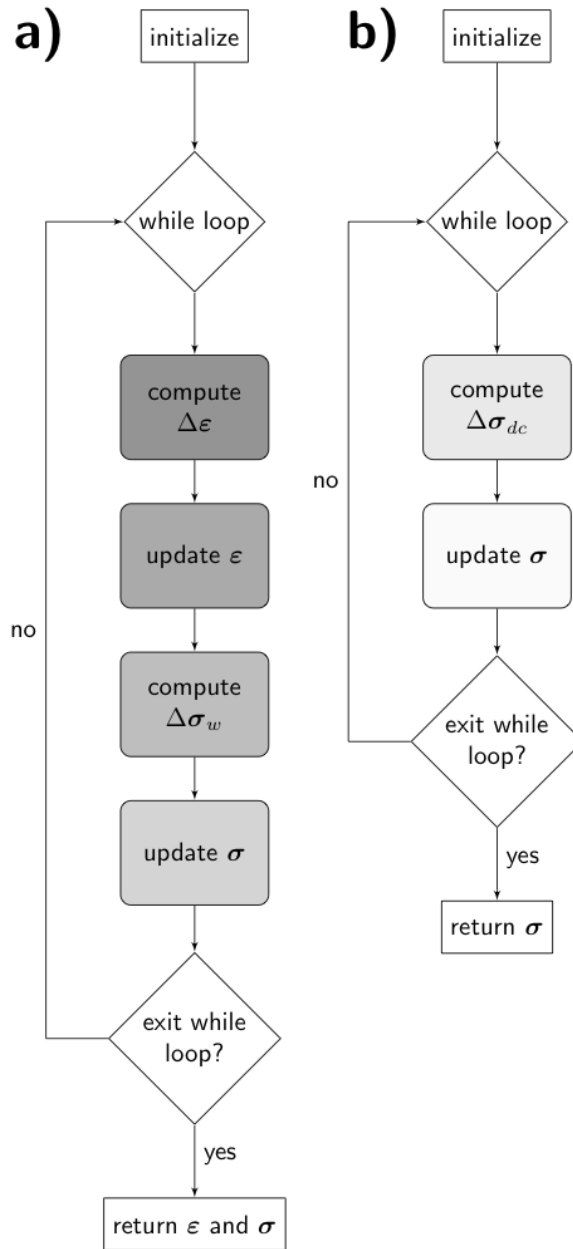


Figure 4: Inversion algorithms for a) GPR and b) ER.

Symbol	Meaning	Note
ϵ	Discretized electrical relative permittivity	Used for GPR and ER
σ	Discretized electrical conductivity	
\mathbf{L}	Discretized differential operator	
\mathbf{s}	Discretized source	
\mathbf{M}	Discretized measuring operator	
\mathbf{d}	Synthetic data	
\mathbf{e}	Residual of synthetic vs observed data	
Θ	Objective function	
\mathbf{v}	Discretized adjoint field	
\mathbf{g}	Gradient of objective function	
α	Step size for \mathbf{g}	
κ	Perturbation parameter used to find α	
m	Momentum parameter	
\mathbf{u}	Electric wavefield on the y component	Only GPR
$\dot{\mathbf{u}}$	Finite-difference time derivative of \mathbf{u}	
$\hat{\epsilon}$	Perturbed permittivity	
$\Delta\sigma_w$	GPR conductivity update	
$\Delta\epsilon$	GPR permittivity update	
$\Delta\epsilon_{\bullet}$	GPR permittivity update from the previous iteration	
φ	Discretized electric potential	Only ER
\mathbf{S}_{dc}	The matrix $-(\nabla_{\sigma}\mathbf{L}_{dc})\varphi^{\top}$	
$\hat{\sigma}$	Perturbed conductivity	
$\Delta\sigma_{dc}$	ER conductivity update	
$\Delta\sigma_{dc\bullet}$	ER Conductivity update from previous iteration	
$\Delta\sigma$	Joint conductivity update	Used for the joint update
a_w	Weight to regulate $\Delta\sigma_w$	
a_{dc}	Weight to regulate $\Delta\sigma_{dc}$	
h	Weight to regulate a_w and a_{dc}	
c	Step size for $\Delta\sigma$	

Table 2: Reference for the notation used in the discretized inverse problems. Symbols common in both GPR and ER experiments are stripped from their subscripts to avoid clutter.

a)

Joint conductivity update $\Delta\sigma$

- Compute a_w and a_{dc} with current h .
- Normalize $\Delta\sigma_w$ and $\Delta\sigma_{dc}$ by their largest amplitude and compute their geometric mean c .
- Compute $\Delta\sigma$,

$$\Delta\sigma = a_w \Delta\sigma_w + a_{dc} \Delta\sigma_{dc}.$$

- Normalize $\Delta\sigma$ by its largest amplitude and set,

$$\Delta\sigma \leftarrow c \Delta\sigma$$

- Check conditions (1)-(4) and update h .

b)

Conditions regulating h

(1) If a_{dc} is decreasing,

$$h \leftarrow \dot{a}_{dc} h.$$

(2) If a_w decreases,

$$h \leftarrow \dot{a}_w h.$$

(3) If the value of Θ_{dc} increases,

$$h \leftarrow \dot{\Theta}_{dc} h.$$

(4) If the value of Θ_w increases,

$$h \leftarrow \dot{\Theta}_w h.$$

Where \dot{a}_{dc} , \dot{a}_w , $\dot{\Theta}_w$ and $\dot{\Theta}_{dc}$ satisfy,

$\dot{a}_{dc} > 1$	$\dot{a}_{dc} \dot{\Theta}_{dc} \dot{\Theta}_w > 1$
$\dot{\Theta}_{dc} > 1$	$\dot{a}_{dc} \dot{\Theta}_w > 1$
$\dot{a}_w > 1$	$\dot{a}_w \dot{\Theta}_{dc} \dot{\Theta}_w > 1$
$\dot{\Theta}_w < 1$	$\dot{a}_w \dot{\Theta}_w \leq 1$

Figure 5: Algorithm for computing the update $\Delta\sigma$ as explained in Section **Joint Inversion**.

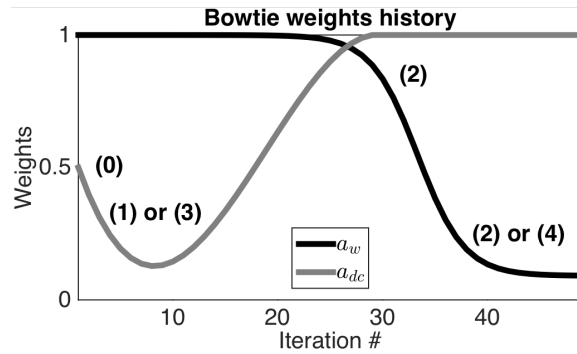


Figure 6: Diagram of weights a_w and a_{dc} as a function of iterations. An initial value for a_{dc} is chosen following condition **(0)**. If a_{dc} decreases over iterations, or Θ_{dc} increases, condition **(1)**, or **(3)**, are activated to increase a_{dc} . Once a_{dc} reaches the value 1, a_w is forced to steadily decrease with condition **(2)**. If $\Theta_{w,\sigma}$ increases over iterations, condition **(4)** is activated and a_w is increased but regulated by condition **(2)**.

—

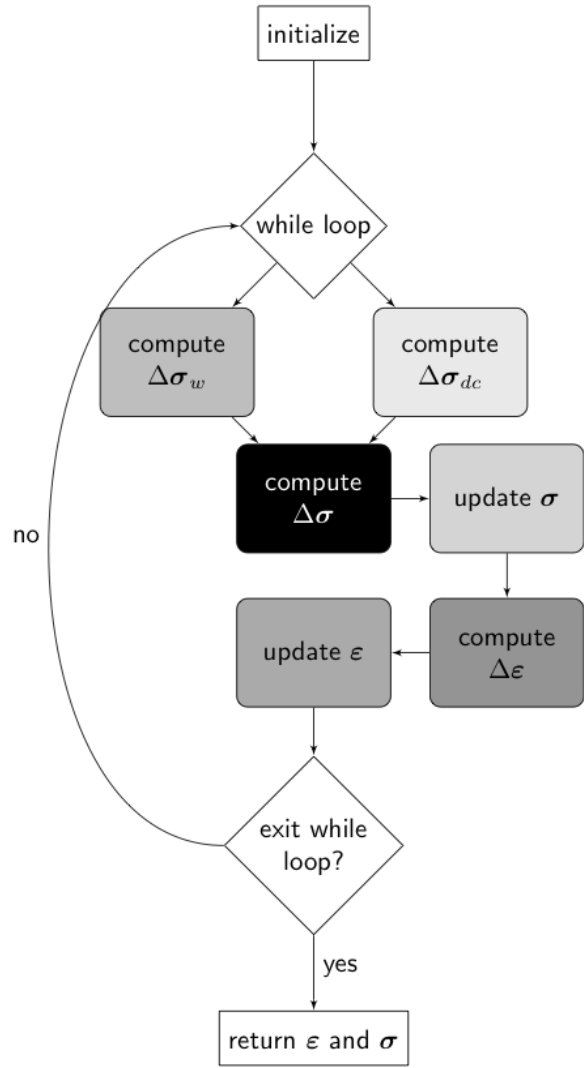


Figure 7: Joint inversion algorithm as explained in Section **Joint Inversion**.

Parameter	Role	Turn-on
initial a_{dc}	Initial weight on $\Delta\sigma_{dc}$	Only in first iteration
\dot{a}_{dc}	Increase h and a_{dc}	Only when $a_w = 1$
\dot{a}_w	Increase h , decrease a_w	Only when $a_{dc} = 1$
$\dot{\Theta}_{dc}$	Increase h , weigh $\Delta\sigma_{dc}$ more	Always
$\dot{\Theta}_w$	Decrease h , weigh $\Delta\sigma_w$ more	Always

Table 3: Parameters for our joint inversions that were found empirically and remained fixed throughout the inversions. An increase in h favors $\Delta\sigma_{dc}$ more than $\Delta\sigma_w$. Conversely, a decrease in h favors $\Delta\sigma_w$ more than $\Delta\sigma_{dc}$.

Parameter	Low σ	High σ
initial a_{dc}	0.85	0.9
\dot{a}_{dc}	4	2
\dot{a}_w	2	1.5
$\dot{\Theta}_{dc}$	6	20
$\dot{\Theta}_w$	0.9	0.9

Table 4: Inversion parameters used for the low and high-conductivity scenario.

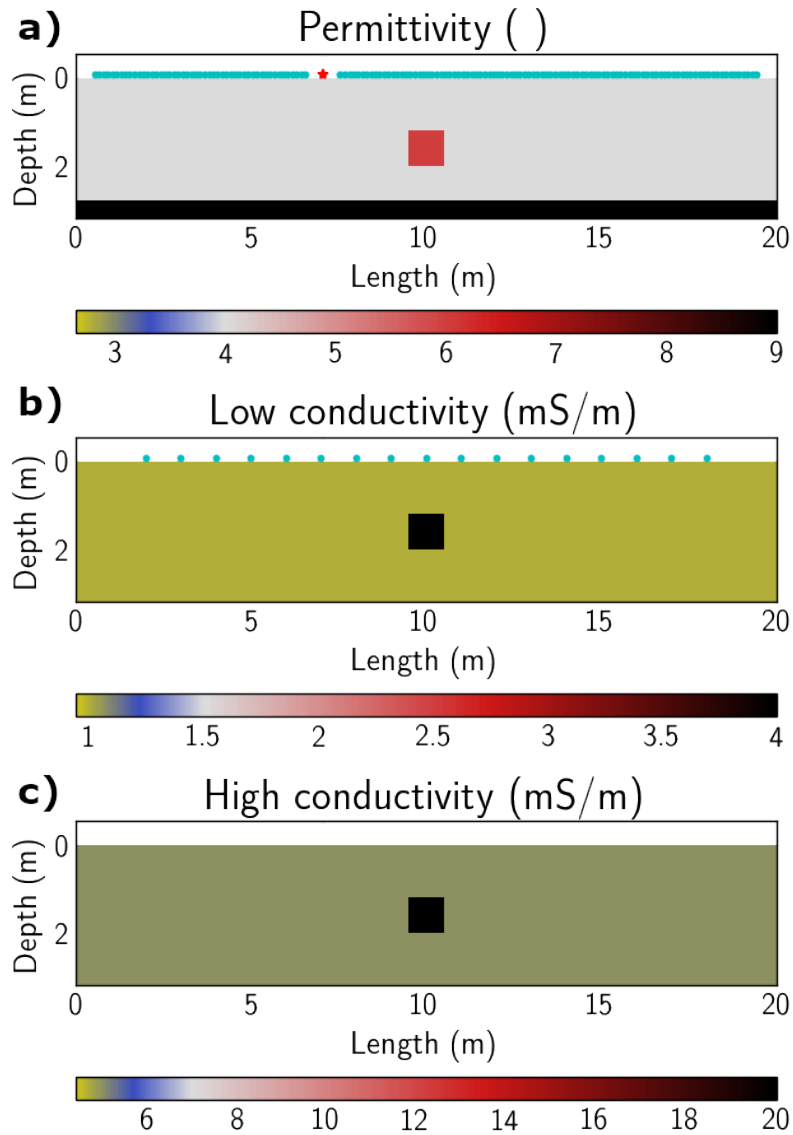


Figure 8: Subsurface models used for our inversions. The size of the box is 1×1 m. **a)** The permittivity background, bottom reflector and box have values of 4, 9 and 6 respectively. The conductivity background and box have values of 1 and 4 mS/m for the low conductivity **b)** and 4 and 20 mS/m for the high conductivity **c)** respectively. An example of GPR receivers and source are depicted in green and red in **b)** and ER electrodes are depicted in green in **c)**.

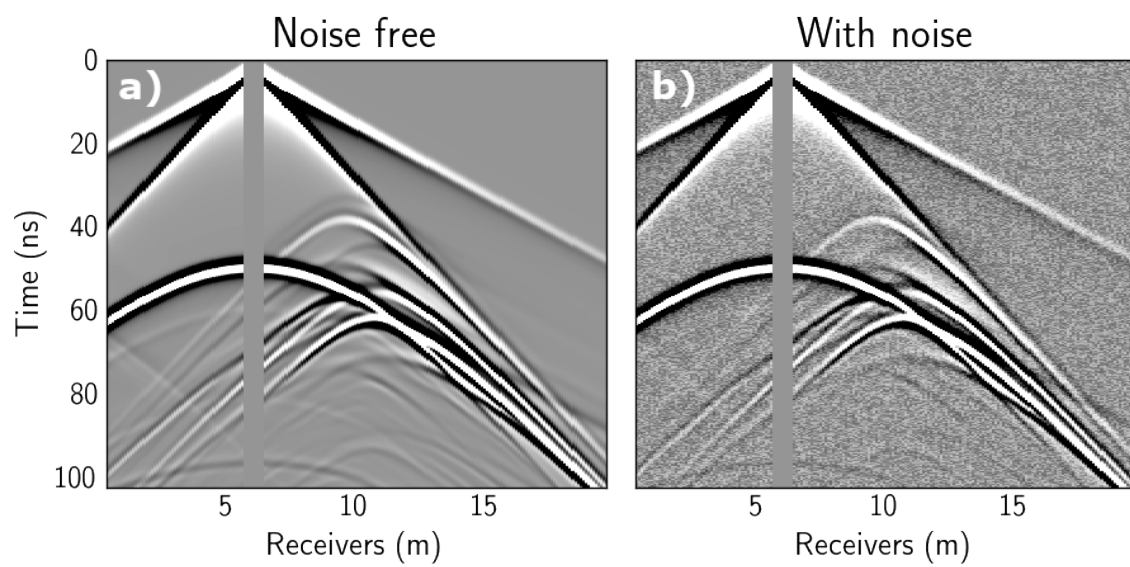


Figure 9: GPR data for one source noise free and with added noise.

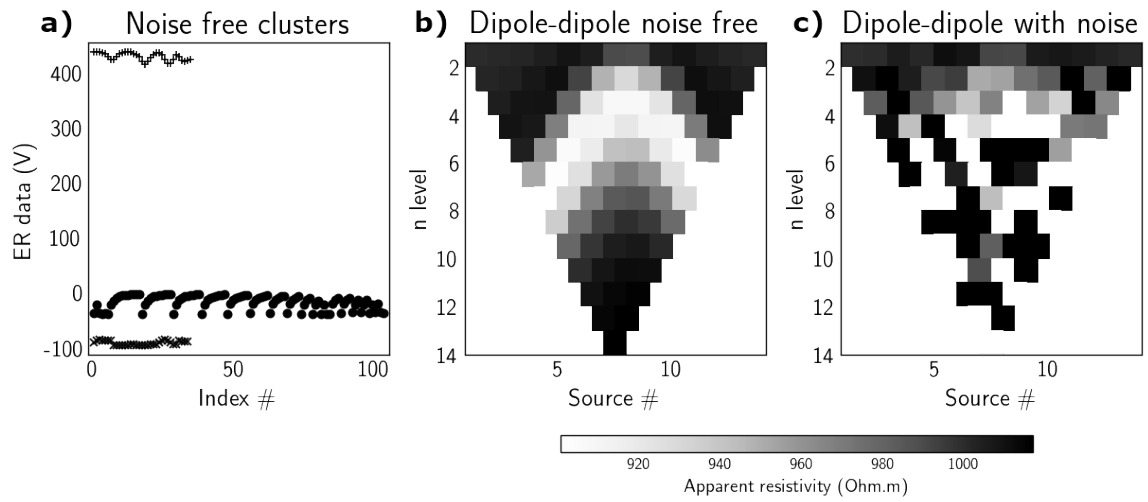


Figure 10: **a)** All ER data noise free and the clusters used for adding noise depicted with symbols +, •, and ×. **b)** Pseudo-section of a dipole-dipole survey noise free and **c)** with added noise.

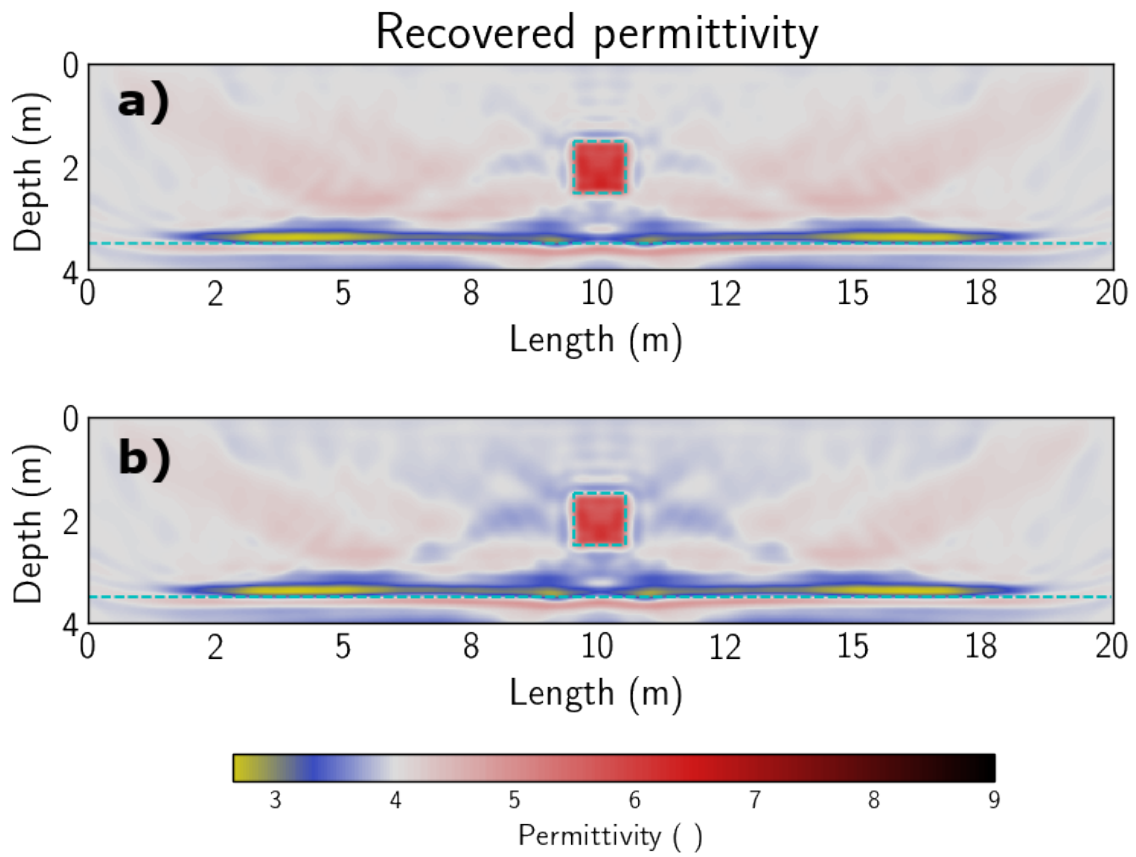


Figure 11: Recovered permittivity for the low-conductivity scenario with just GPR data **a)** and with GPR and ER data **b)**.

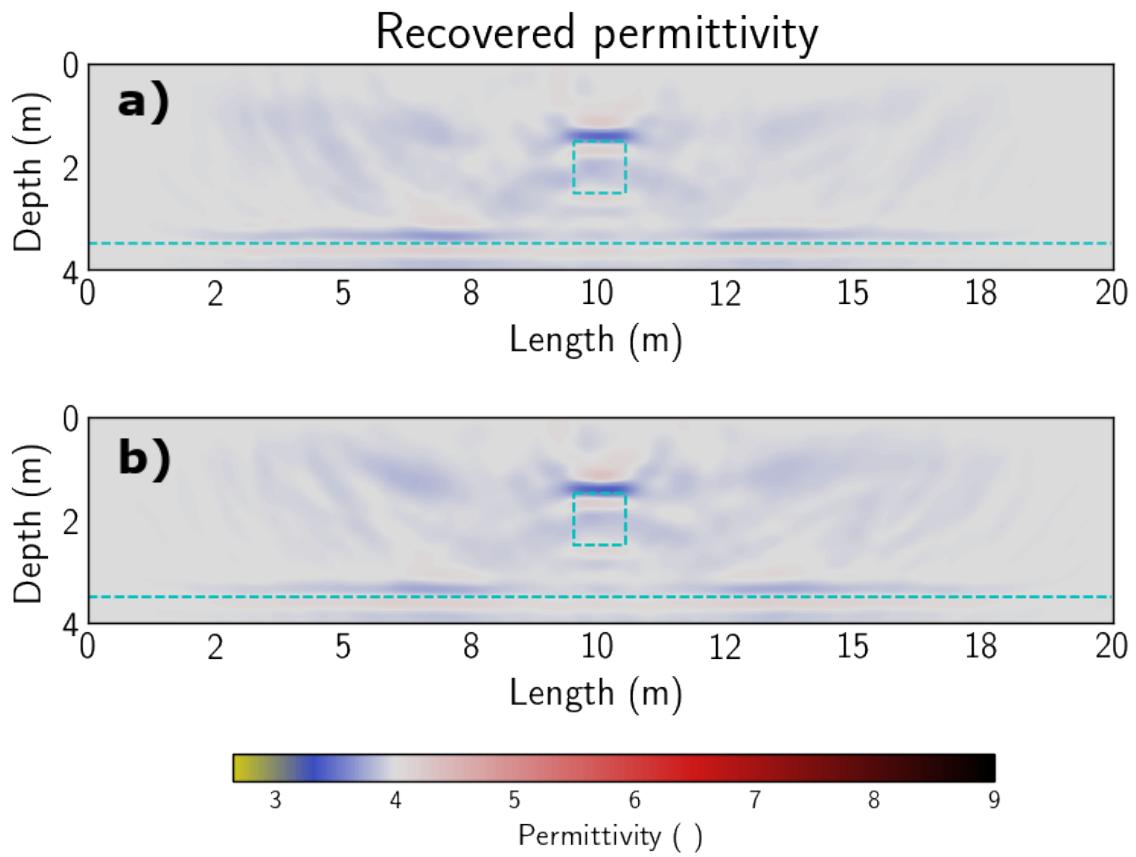


Figure 12: Recovered permittivity for the high-conductivity scenario with just GPR data **a)** and with GPR and ER data **b)**.

–

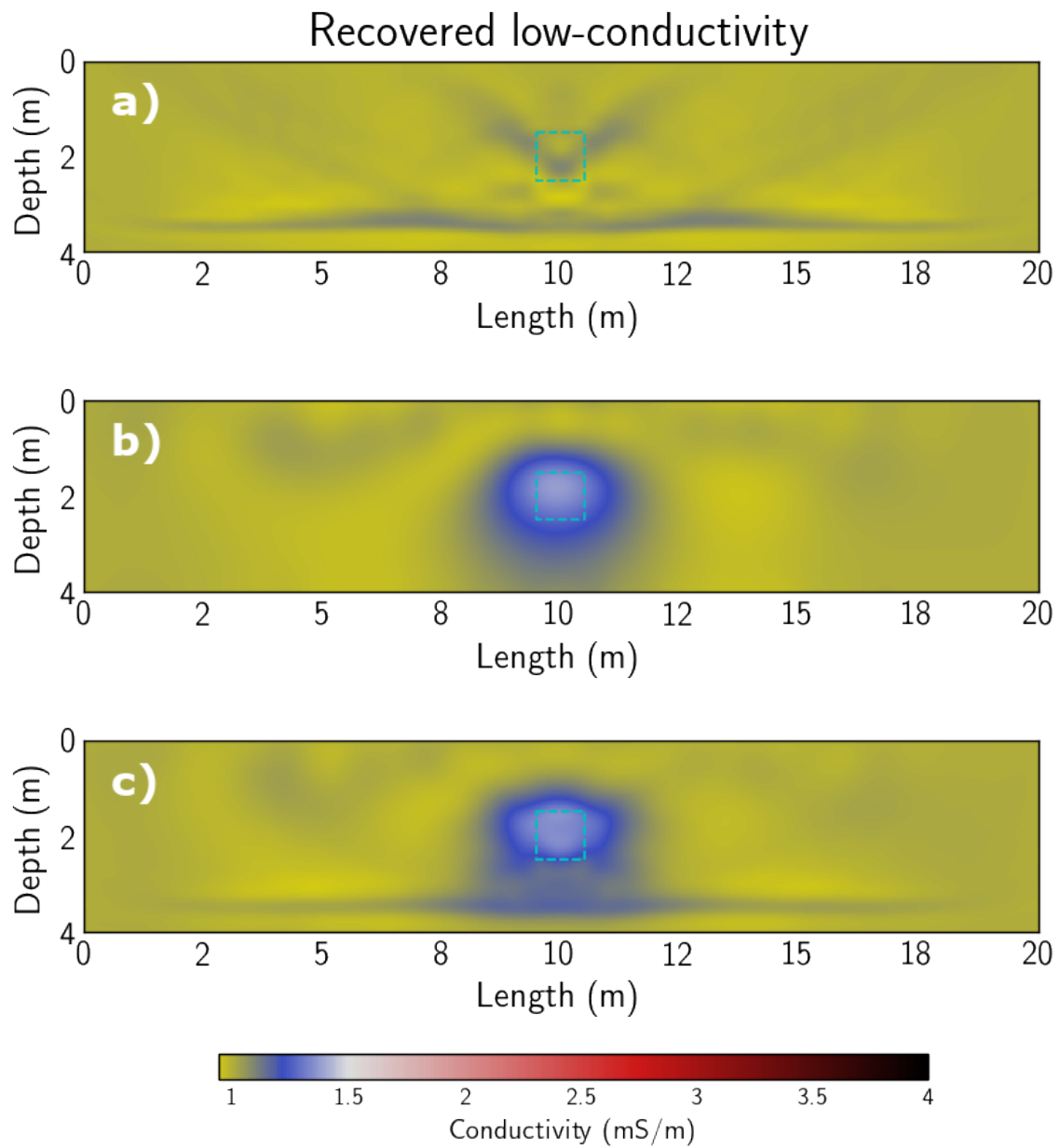


Figure 13: Recovered low conductivity using **a)** just GPR data, **b)** just ER data, and **c)** both GPR and ER data. Each inversion was run for 50 iterations.

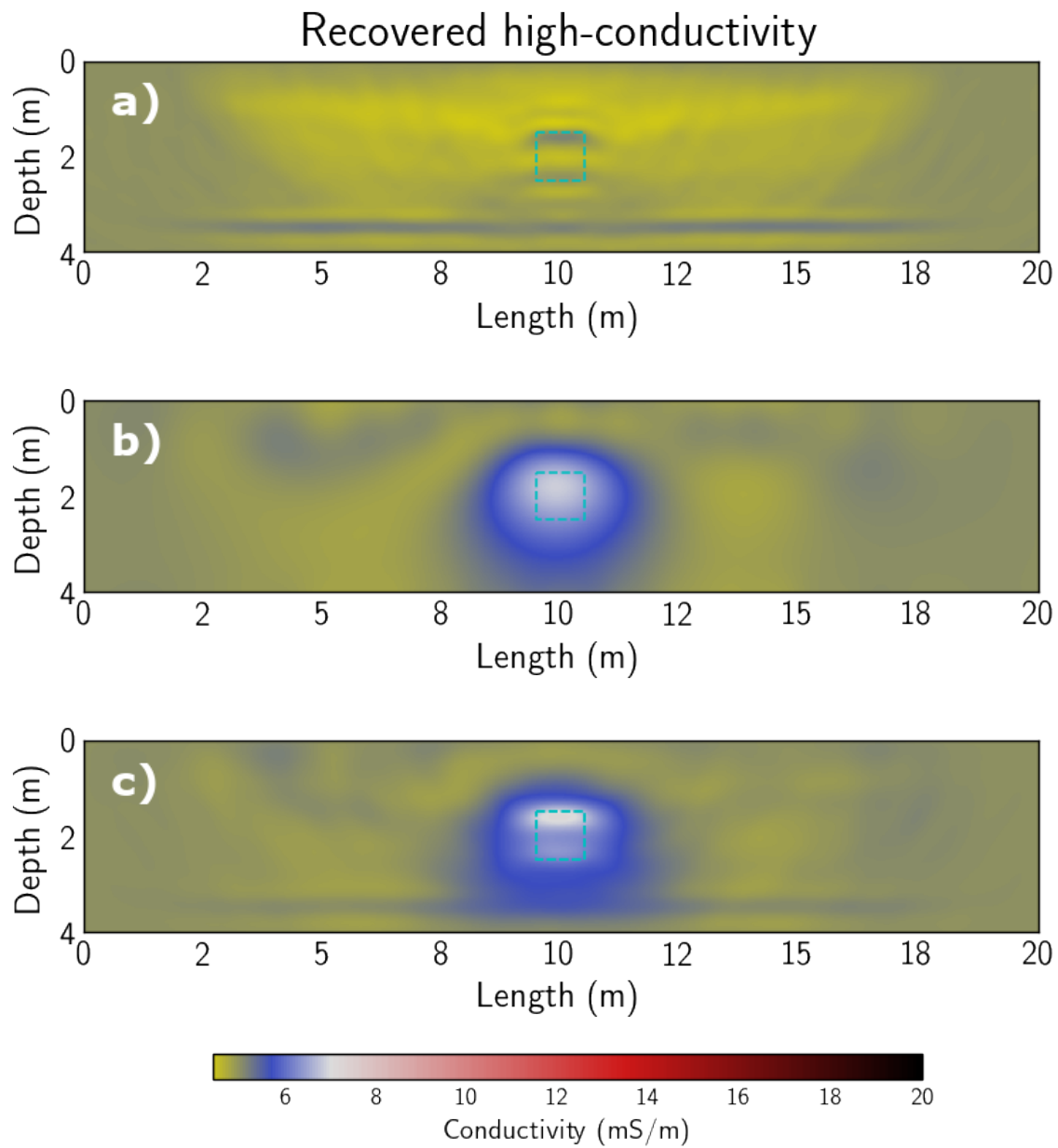


Figure 14: Recovered high conductivity using **a)** just GPR data, **b)** just ER data, and **c)** both GPR and ER data. Each inversion was run for 50 iterations.

Inversion	low σ	high σ
GPR	0.8685	0.8432
ER	0.8964	0.8963
Joint	0.8975	0.8974

Table 5: Ratio of maximum zero-lag cross-correlation between recovered and observed parameters for the low and high-conductivity scenarios. Closer to 1 is better. The joint inversion outperforms the GPR and ER recovered conductivities.

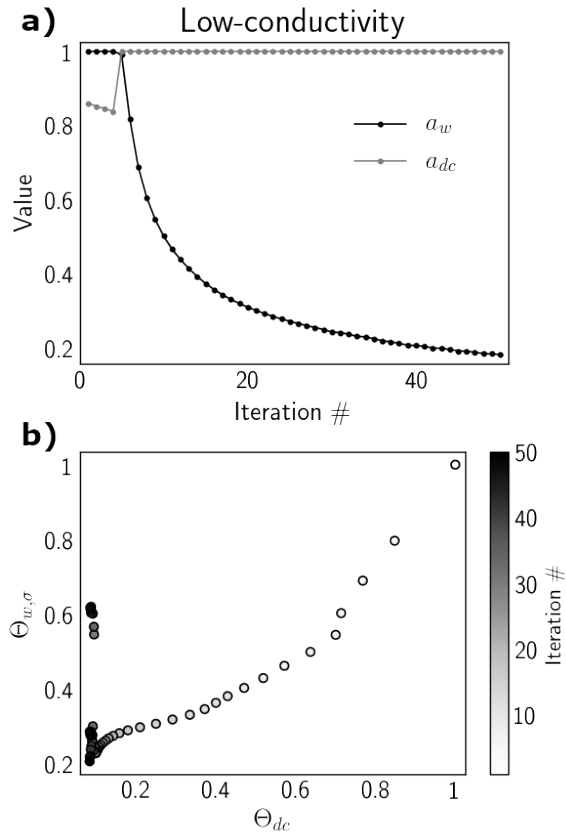


Figure 15: Update weights history over iterations for the low-conductivity scenarios **a)** and normalized objective functions history over iterations **d)**.

—

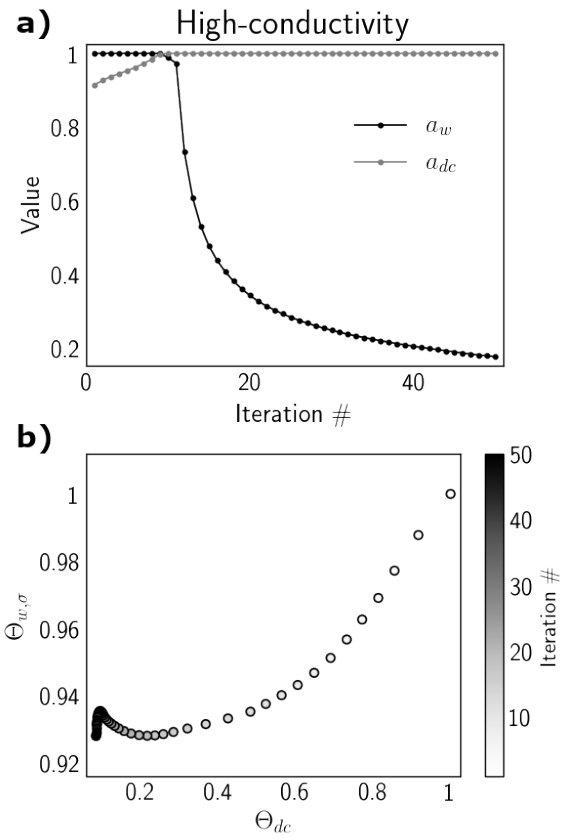


Figure 16: Update weights history over iterations for the high-conductivity scenarios **a)** and normalized objective functions history over iterations **d)**.

—